Lawrence Berkeley National Laboratory

Title

Black Drum Fish Teeth: Built for Crushing Mollusk Shells

Permalink

https://escholarship.org/uc/item/2bd2d8n8

Authors

Deng, Zhifei

Loh, Hyun-Chae

Jia, Zian

et al.

Publication Date

2022

DOI

10.1016/j.actbio.2021.10.023

Peer reviewed

Black Drum Fish Teeth: Built for Crushing Mollusk Shells

Zhifei Deng[1], Hyun-Chae Loh[2], Zian Jia[1], Cayla A. Stifler[3], Admir Masic[2], Pupa U. P. A. Gilbert[3,4], Ron Shahar[5], Ling Li[1]^

[1] Department of Mechanical Engineering, Virginia Polytechnic Institute of Technology and State University, Blacksburg, VA 24060, USA

[2] Department of Civil and Environmental Engineering, Massachusetts Institute of Technology, Cambridge, MA 02139, USA

[3] Department of Physics, University of Wisconsin-Madison, Madison, WI 53706, USA

[4] Lawrence Berkeley National Laboratory, Chemical Sciences Division, Berkeley, CA 94720, USA

[5] Koret School of Veterinary Medicine, The Hebrew University of Jerusalem, Israel

^ Corresponding author: lingl@vt.edu

Abstract

With an exclusive diet of hard-shelled mollusks, the black drum fish (*Pogonias Cromis*) exhibits one of the highest bite forces among extant animals. Here we present a systematic microstructural, chemical, crystallographic, and mechanical analysis of the black drum teeth to understand the structural basis for achieving the molluscivorous requirements. At the material level, the outermost enameloid shows higher modulus (E_r = 126.9 ± 16.3 GPa, H = 5.0 ± 1.4 GPa) than other reported fish teeth, which is attributed to the stiffening effect of Zn and F doping in apatite crystals and the preferential co-alignment of crystallographic *c*-axes and enameloid rods along the biting direction. The high fracture toughness (K_c = 1.12 MPa·m$^{1/2}$) near outer enameloid also promotes local yielding instead of fracture during crushing contact with mollusk shells. At the individual-tooth scale, the molar-like teeth, high density of dentin tubules, enlarged pulp chamber, and specialized dentin-bone connection, all contribute to the functional requirements, including confinement of contact compressive stress in the stiff enameloid, enhanced energy absorption in the compliant dentin, and controlled failure of tooth-bone composite under excessive loads. These results show that the multi-scale structures of black drum teeth are adapted to feed on mollusks.
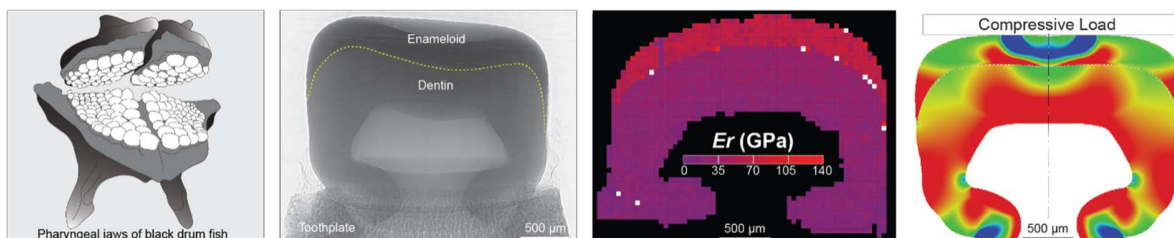
Statement of significance

The black drum fish feeds on hard-shelled mollusks, which requires strong, tough, and wear-resistant teeth. This study presents a comprehensive multiscale material and mechanical analysis of the black drum teeth in achieving such remarkable biological function. At microscale, the fluoride- and zinc-doped apatite crystallites in the outer enameloid region are aligned perpendicular to the occlusal surface, representing as one of the stiffest biomineralized materials found in nature, while these apatite crystals are arranged into intertwisted rods with crystallographic misorientation in the inner enameloid region for increased crack resistance and toughness. At macroscale, the molariform geometry, the two-layer design based on the outer enameloid and inner dentin, enlarged pulp chamber and the underlying strong bony toothplate work synergistically to contribute to the teeth's crushing resistance.

1. Introduction

With over 30,000 species on the planet, fish are a successful group of vertebrates that adapt to different water environments, fresh or salt, scalding-hot or ice-cold. This leads to diverse variations in fish morphology, coloration, physiology, and behavior, offering extensive models for biomimetic engineering designs for materials [1], surface engineering [2], optics [3], and robotics [4]. For example, some fish scales (*e.g.*, elasmoid scales found in teleosts and ganoid scales found in alligator gars and gray bichir) provide important lessons for designing flexible protective material systems, and others (e.g., placoid scales of cartilaginous fish, such as sharks and rays) offer new insights for engineering surfaces with reduced drag and antifouling effects [5–7].

Considering the vast variety of diet types and feeding behaviors, fish teeth also exhibit a remarkable diversity in terms of morphology, composition, and mechanical properties, which could offer important design lessons for the development of novel structural materials. In particular, durophagous fish are those feeding on hard-shelled or exoskeleton-bearing organisms, *e.g.*, mollusks, crabs, and corals [8]. In fact, many fish exhibit durophagous behaviors, including sharks, triggerfish, and some teleost fish [9]. Among all types of durophagy, mollusk crushing represents one of the extreme forms [8]. The durophagous behavior uses a "crushing" system strong enough to withstand heavy loads and durable enough for repetitive loading. For example, horn sharks (*Heterodontus philippi*) and bonnethead sharks (*Sphyrna tiburo*) develop molariform teeth and powerful jaws, while queen triggerfish (*Balistes vetula*) have specialized jawed mouth with teeth for crushing mollusks [9].

In comparison to cartilaginous fish (*e.g.*, sharks, rays, and skates), teleost fish have relatively smaller body sizes/weights. They have evolved a specialized adaption, *i.e.*, the pharyngeal jaws, a "second set" of bony jaws in the throat for durophagous feeding [10,11]. A representative example is the black drum *Pogonias cromis* (Family Sciaenidae), a molluscivorous teleost that is commonly found in the estuarine and shallow marine waters along the Atlantic coast from New England to Argentina [12]. As the second-largest durophagous teleost fish (second to the Indo-Pacific humphead Maori wrasse *Cheilinus undulatus*), the black drum fish preys on mollusks and crabs with its powerful pharyngeal jaws and associated musculature [11,13]. The black drum's pharyngeal jaws consist of two separated upper pharyngeal jaws (UPJ) and a massive lower jaw (LPJ), which are located inside the throat of the fish (**Fig. 1A-D**). The related non-molluscivorous red drum (*Sciaenops ocellatus*, Family Sciaenidae), unlike the black drum, has much smaller UPJs and an arrow-like LPJ with smaller teeth [14]. In addition, their jaw movements during feeding are different; the black drum crush the mollusk shells by squeezing UPJ and LPJ

simultaneously to maximize the crushing force along the vertical direction (yellow arrows in **Fig. 1A,B**), while the red drum shreds weaker-shelled preys (*e.g.*, crabs) by additional retraction of the UPJ [8]. After crushing the mollusk shells with their powerful pharyngeal teeth, the black drum may reject the crushed shell material orally or allow them to pass through the digestive system [12]. Previous studies estimated that *P. cromis* is responsible for processing over one million kilograms of shell material per year from the species' feeding activity in Texas bay [12].

During feeding, the black drum fish's jaws and teeth can generate biting forces up to 300-600 N/kg of its bodyweight; upon reaching the largest body size of 60 kg, the black drum is expected to generate bite forces up to 11,000 N [13]. To compare the bite forces among different species, bite force quotient (*BFQ*) is often used as a metric (Supplementary Note 1) [15–17]. The organisms with above-average *BFQ* are therefore believed to have more powerful teeth and masticatory apparatus. Based on the comparative results, the black drum has one of the highest *BFQ* values among all fish species (~108-130, Table S1, and **Fig. 1E**) [13,16,18,19]. If this comparison is extended to other vertebrates (*e.g.*, mammals, birds, and reptiles), the black drum and durophagous fish in general still own advantageous positions, suggesting their effective designs of the masticatory apparatus when scaled to the same body sizes (**Fig. 1F** and Table S1-S4).

As the black drum fish, as well as many other durophagous fish, developed pharyngeal jaws to crush the hard mineralized mollusk shells during feeding, understanding the structure-property relationship of the tooth material may provide important lessons for novel structural composite designs against heavy contact loadings. However, current studies on the black drum pharyngeal teeth primarily focused on the biomechanics during feeding, *i.e.*, how jaw movements generate high crushing forces [8,13,14]. There has been limited investigation on the black drum pharyngeal teeth from the perspective of material science, particularly the multiscale material design strategies for achieving resistance to high crushing forces and local contact damage and wear.

In this work, we aim to investigate the structural basis of the black drum teeth at multiple length scales, which enable the capability of durophagous feeding by crushing mollusk shells. The fully matured teeth are characterized from multiple perspectives, including microstructural and crystallographic analysis based on electron microscopy and polarization-dependent imaging contrast (PIC) mapping, chemical analysis based on Raman spectroscopy (RS) and energy-dispersive X-ray spectroscopy (EDS), multi-scale mechanical characterizations including nanoindentation, *in-situ* mechanical tests coupled with X-ray micro-computed tomography (μCT), compression tests on individual teeth, and finite element (FE) modeling. Our systematic analysis reveals that the black drum fish teeth exhibit multiscale strategies which adapt to the durophagous diet.

2. Materials and methods

2.1. Materials and sample preparation

The black drum fish heads were obtained from two companies, Pacific Seafood San Antonio, and Fruge Seafood, both from Texas, USA. These fish heads were preserved with ice and kept in fresh condition upon arrival. After separating the pharyngeal jaws and cleaning up the remaining flesh/tissues, these teeth and bony toothplates were kept in frozen condition before further sample preparation.

The pharyngeal jaws were defrosted in water and dried in the air for weeks. To obtain complete units

of mature and immature tooth, the wheel saw was used to cut the bottom bony part. The immature teeth could then be collected easily as they are not connected to the surrounding bone. Afterwards, the individual unit of mature teeth (tooth + the toothplate) was separated by cutting the bone between adjacent teeth.

The selected mature and immature teeth were sonicated in deionized (DI) water to remove the debris thoroughly. After drying, these teeth were mounted and embedded in a room temperature cured epoxy (Epo-Fix, Electron Microscopy Sciences). Samples were polished either horizontally (perpendicular to the biting direction of the teeth) or vertically (parallel to the biting direction) using a polishing machine (MultiPrep^{TM} System, Allied High Tech Products, Inc.) with diamond lapping films stepwise (15 µm, 9 µm, 6 µm, 3 µm, and 1 µm), and finally with 40 nm colloidal silica suspension on a polishing cloth.

2.2. Raman spectroscopy (RS) measurement

A confocal Raman micro-spectroscopy system (WITec, Ulm, Germany) was used to obtain the Raman images. The system was equipped with an Nd:YAG 532 nm laser, 20x Zeiss objective (N.A. = 0.4), a 600 g/mm grating UHTS Raman Spectrometer (WITec, Germany), and a CCD-camera cooled to -60 °C. The excitation wavelength was calibrated by matching the T2g mode peak of a silicon wafer to 520 cm-1. Raman maps of a 100×2400 µm^2 scan area (25×600 points) were acquired with a continuous laser beam with an accumulation time of 0.5 seconds per point with a pre-bleaching time of 0.5 seconds. WITec Project Five, MATLAB, and Origin Pro 9 software were used for image processing and analyses. Cosmic ray removal and background subtraction were performed to increase the signal-to-noise ratio. The phosphate ν1 peak was fitted with a Lorentzian function, and the peak position, width, and intensity were extracted from the fit for further analyses. The average peak position and width of the ν1 peak at the same distance from the teeth surface are computed and plotted against the distance.

2.3. Scanning Electron Microscopy (SEM)

Dried teeth samples were coated with a Pd/Pt layer with the thickness of 10 nm to reduce charging effects prior to electron microscope imaging. SEM images were then acquired with a field-emission SEM (LEO 1550, Zeiss, Oberkochen, Germany) with an acceleration voltage of 5 kV and a working distance of ~7 mm. To reveal the microstructures and the crystallite alignments, slight etching was applied to the fine polished surface by using 1% formic acid for 1 min before SEM imaging.

2.4. Energy-dispersive X-ray spectroscopy (EDS) measurement

SEM-EDS data was obtained using a scanning electron microscope (Vega3, Tescan, Brno, Czech Republic) in variable pressure mode (20 Pa, gas: N2, accelerating voltage: 20 keV). The backscattered electron (BSE) images were acquired with a YAG crystal scintillator-based detector. The EDS maps were acquired with a Bruker XFlash 630 silicon drift detector with sufficient acquisition time to achieve at least 2,000 counts per pixel in the mapped area. The elemental composition is quantified using the Bruker Esprit 2.1 Software with PB Linemarker-ZAF correction. The elemental composition map is normalized with the maximum composition for improved contrast. The average mass percentage of each element at the same distance from the teeth surface is computed and then plotted against the distance.

2.5. Polarization-dependent imaging contrast (PIC) mapping

A vertical cross-section of a mature tooth was prepared by serial polishing, cleaning, and air-dried. Before PIC mapping, the selected areas of interest were coated with 1 nm Pt, while the rest of the surface was coated with 40 nm Pt using a Cressington 208 Series sputter coater (Cressington Scientific Instruments, Watford, England) equipped with a thickness monitor while spinning and tilting [20]. PIC

mapping was performed using the PEEM3 microscope at the 11.0.1 beamline at the Advanced Light Source (ALS) at Lawrence Berkeley National Lab. A stack of 38 images was acquired at 19 different X-ray polarizations [21–24] with minimal charging [25] and radiation damage [26]; one at 0.2 eV below the Ca L-edge peak 1 and the other at 0.2 eV above peak 1 [27]. The images were imported into PEEMvision and aligned if necessary. The above peak images were digitally divided by the corresponding below peak images to increase the dichroic contrast. Each pixel in the 19-image stack contains intensity versus polarization information that was to a cosine squared, Malus' law relationship. The fit parameters provide the in-plane and out-of-plane angles with respect to the polarization plane of the X-rays that are incident from the right at an angle of 30° from the vertically mounted sample surface. The in-plane angles are displayed by the hues assigned in the color bar. The out-of-plane angles are displayed such that crystals oriented directly into the x-rays (completely out of the polarization plane) are black and crystals that are oriented completely within the polarization plane are full brightness. PIC maps were created from the 19-image stack using the GG macros. For each area, 9 overlapping, individual PIC maps were acquired in a 3×3 array and were stitched together in Adobe Photoshop CC 2021.

2.6. Instrumented nanoindentation

Load-controlled nanoindentation was performed on the vertically polished sample surfaces for the areal and line mapping using Micro-Materials instrumented nanoindentation system (NanoTest Vantage platform 4) and a Berkovich tip (trigonal pyramid, semi-angle of 65.3°). Typical load functions include loading (15 s), holding (10 s) at the maximum load (1 mN), and unloading (15 s), and thermal drifting was monitored when the load was unloaded to 10% of the maximum force for 30 s. The hardness H and indentation modulus E_r were quantified based on the standard Oliver-Pharr (O-P) methodology [28]. For the areal map, the grid spacing between adjacent indents was $30 \times 30 \ \mu m^2$, and in total 6000 indents were conducted to generate the entire map. For the line map, the grid spacing between adjacent indents was 2μm, and 1000 indents were conducted along each line; in total, three lines were conducted. In addition, cube-corner nanoindentations were also performed on horizontally polished enameloid and dentin of mature teeth with increasing maximum loads, *i.e.*, 0.5, 1, 2, 3, 5, 8, 10, 20, 30, 40, 50, 60, 70, 80, 90, 100, 200, 300, 400, and 500 mN. The post indentation residues were imaged using SEM for further analysis.

2.7. Macroscale compression tests

After separating the individual mature teeth, two groups of compression samples were prepared, *i.e.*, mature teeth with/without the underlying bony toothplate. The bottom of the samples was polished until flat and stable. These teeth were kept in 0.9 % NaCl solution overnight for rehydration before testing. Compression tests were conducted using an Instron system (model 5984) at a constant rate of 2 mm/min until the final fracture. The samples were approximated as pillars with irregular cross sections, where the heights were directly measured with a caliper, and the projection-areas (approximated as cross-sectional areas) were estimated from the top-view photos. Subsequently, the nominal stress and strain were calculated.

2.8. Micro-computed X-ray tomography and in-situ mechanical testing

Micro-computed tomography (μCT) was conducted using the synchrotron X-ray imaging at beamline 2BM of the Advanced Photon Source, Argonne National Laboratory, Chicago. The X-ray beam energy used was 27.4 keV with an imaging resolution of 1.725 μm/pixel and the field of view (FOV) of $2560 \times 1024 \ pixel^2$, corresponding to ~4.4 mm in width and ~1.7 mm in height. In addition, *in-situ* mechanical tests were also conducted by using a customized mechanical loading device which enables displacement-controlled loading and simultaneous μCT data acquisition. During each μCT scan, the stage was rotated 180° to obtain 1500 projections for reconstructing the original and deformed structure at each

loading step. A ceramic wedge tip was also used to conduct *in-situ* indentation tests. The samples for *in-situ* tests were further trimmed and polished to make cube-shaped geometries that fit into the FOV. Tomographic reconstructions were performed using TomoPy [29] and rendered with Avizo (Thermo Fisher Scientific, USA).

2.9. Finite element method

The geometric models of the black drum teeth were generated based on the manual tracing and simplification of the SEM and μCT projection images. The FE simulation of the compression tests on an individual tooth (with/without toothplate) was simplified as an axisymmetric 3D problem. The tooth was modeled as a three-phase composite, which consists of an outer enameloid, an underlying dentin, and a supportive bony toothplate, where the contact between the phases is considered as perfectly bonded. All three phases were simplified as isotropic, elastic-perfectly plastic materials using four-node bilinear axisymmetric quadrilateral elements (CAX4R in ABAQUS element library). The material properties of the enameloid and dentin were obtained from Berkovich nanoindentation experiments where $\sigma_y \approx H/2.8$ [30], and the material properties of the bone were taken from literature [31]. Similar simplified estimation of the material models was applied in FE analysis of other biomineralized composites, such as the multilayered design in the ganoid fish scale [32]. The FE results obtained from the simplified models were primarily used to predict the stress-strain distribution (to correlate with the experimental observations from macroscale compression tests) rather than precise prediction of the stress and strain values. In addition, the compression tests were simulated by applying the loading through an upper rigid-body compression plate, where large-deformation theory and frictionless contact between the plates and teeth samples were assumed. The simulation was performed in ABAQUS with the general statics modulus. Mesh convergence was also performed for accurate solutions to the load–displacement curves and stress contours.

2.10. Statistical analysis

Averages and standard deviations were used as the descriptive averages for all the measurements throughout the entire paper wherever possible, including the nanoindentation modulus and hardness (**Fig. 6B**), crack length measurements based on cube-corner indentation (**Fig. 7D**), and macroscale compression tests (**Fig. 8A**, insert table). In addition, the standard deviations of the data were used as error bars in the figures (*e.g.*, **Figs. 6B** and **7D**).

3. Results

3.1. Microstructure

The pharyngeal jaws of black drum, including two UPJs and one LPJ, are positioned symmetrically in the masticatory apparatus (**Fig. 1C,D**). The LPJ is composed of two halves joined by a central suture line (Fig. S1A-D). The individual teeth on the bony toothplates are compactly arranged with a symmetric size distribution with respect to the central line (red dashed line in **Fig. 1D**); specifically, the sizes (measured as the projected areas) of the teeth range between 0.5~30 mm^2, decreasing almost linearly from the central line to the edge region on the LPJ (Fig. S1E). The black drum replaces its teeth throughout its lifetime [11], and the immature teeth are embedded beneath the mature ones and within the bony toothplates, as shown in the cross-sectional optical and scanning electron microscopy (SEM) images (**Fig. 2A,B** and Fig. S1F). Here we define the normal direction "N" as the biting direction, *i.e.*, from bony toothplate to teeth biting surface (yellow arrows in **Fig. 1B**) [8].

In contrast to the canine teeth in the non-molluscivorous red drum [8], the molluscivorous black drum has the molariform teeth with a smooth bowed outer surface (**Fig. 2C,D,F**), while some teeth with pointy tips or needle-like geometries are present at the edges of the toothplates (Fig. S2). Our study here is primarily focused on molariform teeth. The mature molariform teeth are positioned in the bony toothplate through a round connecting rim (yellow dashed region in **Fig.2E**, *ca.* 75 μm in width), which is also highlighted in the top-view reconstruction of the tooth and toothplate (**Fig. 2G**). There are no discernable organics in the contact rim; however, the fibrous organic material-based tissue that connects adjacent dentin and bone is found in the region below (white dashed region in **Fig. 2E**, and Fig. S3) [33]. The immature teeth are enclosed inside a chamber directly underneath individual mature teeth (**Fig. 2A,B**). Unlike the mature teeth whose thickened dentin roots are bound with toothplates, the dentin in immature teeth become thinner towards the root (Fig. S4). Both the mature and immature teeth have smooth outer surfaces, while microscopic feeding-induced abrasion marks were often observed on mature teeth (Fig. S5). As reported previously, the bony toothplate in the pharyngeal jaws of black drum fish exhibits a unique porous microstructure unlike the common trabecular bones observed in other vertebrates [11].

Each tooth of the black drum consists of an outer enameloid layer and an inner dentin layer separated by the dentin-enameloid-junction (DEJ, **Fig. 2A-D**). Backscattered-SEM imaging reveals a higher electron intensity in the enameloid layer in mature teeth, suggesting its higher mineral density than dentin (**Fig. 2B**). The fractured surface of mature teeth further revealed the microstructural difference across the DEJ interface, *i.e.*, the rough and twisted fracture surface in the enameloid and the relatively smooth fracture surface in the dentin, respectively (**Fig. 3A**). The dentin layer consists of uniformly distributed dentin tubules (*ca.* 1 μm in diameter) parallel to the normal direction, where tubule branching is occasionally observed (**Fig. 3B,C**). It should be noted that the dentin tubule density in black drum teeth (*ca.* 2.3×10^5 tubules per mm^2 in inner dentin) is substantially larger than human teeth ($1.37 - 3.23\times10^4$ per mm^2) [34], alligators and crocodiles ($2.1 - 2.2\times10^4$ per mm^2) [35], and some dinosaurs ($0.92 - 1.57\times10^4$ per mm^2) [35], while the tubule diameters are approximately similar in different species.

SEM imaging of the vertically polished cross-section after slight acid etching (see Methods) revealed that the rough fracture surface in the inner enameloid close to DEJ results from the 3D twisted and interlaced enameloid rods, the building units of enameloid (yellow-shaded mask, **Fig. 3F**). These enameloid rods consist of nanorod-like crystals, similar to other fish teeth, *e.g.*, parrot fish teeth [36], and black carp teeth [37]. The diameter of the enameloid rods decreases from DEJ (5-20 μm, **Fig. 3F**) to the outer surface (1-2 μm, **Fig. 3E,G**). SEM images of a horizontally polished and etched surface also show consistent observations (Fig. S6). In addition, the nanorod-like crystallites within individual enameloid rods exhibit discernible crystallographic misorientations (**Fig. 3G**).

3.2. Chemical analysis

The chemical information of the black drum teeth was investigated through correlative RS and EDS analyses (**Fig. 4**).

A high-resolution RS map across the entire tooth thickness direction (yellow box, **Fig. 4A**) and the averaged Raman spectra (**Fig. 4B**) reveal that both enameloid and dentin regions have a phosphate v_1 peak at 959-964 cm^{-1}, indicating that the main mineral phase in both regions is similar to hydroxyapatite (HA, standard peak position *ca.* 961 cm^{-1}) [38]. However, the peak position shifts to higher wavenumbers in enameloid (962-964 cm^{-1}) in comparison to that in dentin (959-961 cm^{-1}) (**Fig. 4C**), which is due to the different chemical environment in the two regions. A similar Raman peak shift has been reported in parrotfish teeth, which was correlated with the change in mineral composition from HA to fluorapatite

(FA) crystals [36]. Quantitative analysis of the width (full width at half maximum, FWHM) of this peak further reveals a broadening effect in the dentin region (**Fig. 4D**), suggesting its lower crystallinity [39]. In addition, the remaining evident peaks in the dentin region indicate the presence of a higher amount of proteinaceous materials (Amide III 1200-1300 cm^{-1}, Amide I 1660-1670 cm^{-1}, and C-H 2850-3300 cm^{-1}, **Fig. 4B**) [40–42], which is most likely collagen, as found in human tooth dentin [43,44] and elephant tusk dentin [45]. Strong fluorescence was observed when conducting RS measurements on immature teeth, due to their higher concentration of organic materials.

Correlative EDS measurement performed on the same sample reveals the major chemical elements and their compositional gradients within the mature teeth (**Fig. 4E-H**). **Fig.4E** summarizes the averaged EDS spectra of the enameloid (blue) and dentin (red), where the distribution of the major elements Ca, F, Mg, and Zn is shown in **Fig. 4F**. Several important features are observed. First, Ca and P are distributed across the entire tooth (**Fig. 4G**), consistent with the RS measurement that apatite is the major mineral phase in both enameloid and dentin regions. Second, a higher concentration of Ca is found near the DEJ (in both inner enameloid and outer dentin), indicating higher mineral density compared to outer enameloid (**Fig. 4F,G**). Third, the trace elements F and Zn are mainly present in the enameloid layer, decreasing from the outer to the inner enameloid, while Mg shows a higher concentration in the dentin layer with an increasing gradient towards the inner dentin (**Fig. 4H**). Table S5 quantifies and compares the EDS results (non-carbon elements) with the theoretical values of HA and FA, from which the mineral phase in the enameloid is estimated to be $Ca_{10}(PO_4)_6(OH)_{0.89}F_{1.11}$ with Zn substitutions (Supplementary Note 2), while the dentin has a mineral phase more similar to HA with Mg substitutions. These conclusions agree well with the RS measurement: the Zn-doped HA/FA crystals in the enameloid layer contribute to the peak shift to higher wavenumbers [38], while Mg substitution in dentin results in the peak shift to lower wavenumbers [46].

3.3. Crystallographic analysis

Polarization-dependent imaging contrast (PIC) mapping techniques were employed to determine the crystallographic orientations of the enameloid crystals. Many anisotropic crystals exhibit dichroism, *i.e.*, peak intensity variations in the X-ray absorption spectra depending on the crystallographic orientations; such dichroism can therefore be used in PIC mapping to visualize and quantify crystal orientations [36]. PIC mapping has been used extensively for carbonates in various biominerals and recently apatites in bone and teeth [36,47,48].

Fig. 5A shows the locations on the polished black drum tooth where two PIC maps were acquired in the outer and inner enameloid regions, respectively. In outer enameloid (*ca.* 50 μm beneath the tooth surface), the enameloid microstructure shows *ca.* 1-2 μm rods aligned approximately perpendicular to the tooth surface, where the cyan and green color indicates that the HA/FA crystals also align their *c*-axes approximately perpendicular to the tooth surface, with slight crystal misorientations among adjacent rods (**Fig. 5B**). When gradually approaching the middle enameloid (bottom portion in **Fig. 5B**), the rods become thicker and more interwoven, where both rod orientations (*e.g.*, rods marked by yellow and white crosses running *ca.* 90° from each other) and crystal orientations (*e.g.*, colors change from cyan to red in adjacent rods) exhibit more significant variations.

In the PIC map acquired in the inner enameloid (*ca.* 300 μm beneath tooth surface), one can observe considerable distributions of rod diameters, between *ca.* 1-5 μm (**Fig. 5C**). At depth close to the DEJ, the rods can branch and interweave with adjacent rods as evident by the abrupt color changes (*e.g.*, rods marked by yellow and white crosses, **Fig. 5C**). Crystallographic misorientations are presented within

individual rods, and similar observations have been reported in many animals' tooth enamel(-oid), including mouse, human, sheep, and parrotfish, which may contribute to crack deflection within individual enameloid rods [47,48]. Many black pixels in the PIC maps are present due to the absence of polarization dependence. These black regions could result from non-polarization dependent material, such as organics, voids, or amorphous materials [36]. However, based on their size, morphology, and similarity to other rods in the PIC map, it is believed that these regions represent the crystals with their *c*-axis parallel to the beam direction.

3.4. Local mechanical properties: modulus and hardness

The local mechanical properties (reduced modulus E_r and hardness H) of the black drum teeth were investigated via instrumented nanoindentation with a Berkovich tip (**Fig. 6**). Nanoindentation mapping of the vertical cross-section of a mature tooth clearly reveals the two-layered enameloid-dentin structure, where the enameloid (H = 2-4 GPa, E_r = 70-110 GPa) is considerably harder and stiffer than the dentin (H = ~1 GPa, E_r = 20-50 GPa) (**Fig. 6A**). Additional high-resolution line mappings (step size, 2 μm) conducted across the entire tooth thickness reveals the presence of mechanical property gradients within both enameloid and dentin regions: gradual increase towards the biting surface in enameloid and gradual decrease towards the tooth interior in dentin (**Fig. 6B**). Further measurements conducted on the pristine enameloid surface (no polishing) revealed H = 5.0 ± 1.4 GPa and E_r = 126.9 ± 16.3 GPa (n = 14) along the biting direction (see the schematic diagram in **Fig. 6C**), in comparison with H = 5.1 ± 1.0 GPa and E_r = 108.3 ± 13.6 GPa measured from the across direction. The measured H and E_r value in the outer enameloid of the black drum are close to the shark teeth enameloid, which both agree with the ranges for HA crystals [49,50], but are smaller than the geological FA crystals (H = 11.3 ± 0.8 GPa, E_r = 148 ± 9 GPa) [51].

Fig. 6C compares the nanomechanical properties of the black drum teeth with other biomaterials in the Ashby plot of modulus *vs*. hardness [36,52]. Remarkably, the black drum tooth enameloid the highest modulus compared to the reported values from other highly mineralized biological materials, where the data scattering, particularly for the "across" orientation, is most probably due to local microstructural variations as observed in **Figs. 3 and 5**. In contrast, H and E_r values of the dentin region range 0.5-1.5 GPa and 20-50 GPa, respectively, comparable with other dentin structures (**Fig. 6B,C**). Moreover, a recent study on parrotfish (*Chlorurus microrhinos*) teeth shows that the modulus ratio of along and across the biting direction for enameloid is $E_{r,along}$ / $E_{r,across}$ = 1.18 [36], close to the modulus ratio of black drum teeth 1.17 (= 126.9 GPa /108.3 GPa) in the present study. In comparison, the reported ranges for the stiffness ratios C_{33}/C_{11} in FA and HA crystals are (1.17-1.33) [53,54] and (1.13-1.40) [54,55], respectively.

3.5. Local mechanical properties: fracture toughness

Nanoindentation with a cube-corner tip was used to characterize the teeth's performance under sharp contact loadings (**Fig. 7**). **Fig. 7A** shows the representative indentation curves on polished enameloid and dentin surfaces along the biting direction at maximum loads of 50, 200, and 500 mN (see all curves in Fig. S8). The corresponding indentation residues on the enameloid and dentin regions are shown in **Fig. 7B,C**, respectively. At the same maximum loads, the indentation depths and residue sizes are significantly larger in dentin than in enameloid, as expected by their hardness contrast. In addition, the indentation curves of enameloid exhibit "pop-in" events (black arrows, **Fig. 7A** inset), which were caused by the discrete crack formation (see the corresponding 50 mN indentation residue in **Fig. 7B**). In contrast, dentin exhibits plasticity-like deformation even at the highest load, where the dentin tubules were highly deformed and no significant cracking was observed (**Fig. 7C**).

Based on contact mechanics, the indentation residue sizes a is related to the maximum load P and the hardness H through the following relationship

$$a = \left(\frac{P}{\alpha H} \right)^{1/2} \quad (1),$$

where α is a non-dimensional geometric constant for the indentation tip ($\alpha = 1.30$ for three-sided Berkovich and cube-corner tips) [56]. Moreover, when the indentation load is sufficiently high, cracks will originate from the indentation edges, and their size c is given by

$$c = \left(\frac{E}{H} \right)^{1/3} \left(\frac{\chi P}{K_c} \right)^{2/3} \quad (2),$$

where E is the elastic modulus, χ is a nondimensional constant ($\chi = 0.04$ for a cube-corner tip) [57]. Therefore, the fracture toughness K_c can be estimated as [58]

$$K_c = \chi \left(\frac{E}{H} \right)^{1/2} \left(\frac{P}{c^{3/2}} \right) \quad (3).$$

In the present study, 10 indentations were conducted at each load from 0.5-500 mN, and a and c were directly measured from the post-indentation SEM images. As shown in **Fig. 7D**, we confirm that the a-P and c-P profiles have the predicted slopes of 1/2 and 2/3, respectively. Moreover, K_c of the black drum teeth enameloid is estimated as 1.12 MPa·m$^{1/2}$ (Supplementary note 3), which is higher than that of FA crystal (0.76 ± 0.13 MPa·m$^{1/2}$) [59] and comparable to HA crystal (1.20 ± 0.23 MPa·m$^{1/2}$) [60] and human tooth enamel (0.7-1.3 MPa·m$^{1/2}$) based on indentation experiments [61,62].

We further evaluated the fracture resistance of enameloid by calculating the cumulative frequency of cracking (f) under different loads (**Fig. 7E** and Supplementary note 4) [36,56,63]. When compared to previously measured biomineral composites such as spearers (*Lysiosquilla*) and smashers (*Odontodactylus*) in mantis shrimp [63], and the parrotfish teeth (*C. microrhinos*) [36], the black drum teeth enameloid exhibits a higher fracture resistance (*i.e.*, larger loads required to initiate cracks at $f =$ 50%) (**Fig. 7E**). The only exception, sponge biosilica (*Monorhaphis chuni*), on the other hand, achieves its superior toughness through its laminated design [56].

3.6. Macroscopic mechanical behavior: experimental analysis

To investigate the teeth's macroscopic mechanical behavior, compression tests were conducted on individual mature teeth with and without bony toothplates (**Fig. 8A-C**). The failure loads for individual teeth range between 150 and 600 N depending on the sizes (Fig. S8). The representative nominal stress-strain curves for the two groups of samples are shown in **Fig. 8A**. Typically, the teeth with bony toothplates experience three distinct deformation stages: toothplate deformation and failure, tooth repositioning, and tooth deformation and failure (**Fig. 8A,B**). In contrast, the detailed deformation process of the teeth is revealed by the tests for samples without bony toothplates, which involves initial fracture via vertical cracking (**Fig. 8C**-i), horizontal cracks connecting adjacent vertical cracks (**Fig. 8C**-ii), and final collapse (**Fig. 8C**-iii).

The normalized failure strength of the teeth ($\sigma_{\text{teeth}} = 33.8 \pm 12.2$ MPa) is significantly higher than the bony toothplate ($\sigma_{\text{bone}} = 22.1 \pm 5.9$ MPa), while the deformation of the latter contributes to *ca.* 50% of the total energy dissipation (W) (**Fig. 8A**, inset table). This result suggests two important mechanical functions of the toothplates: (1) under normal crushing/impact loads, the toothplates provide support/base for the teeth and energy absorption, and (2) under excessive loads, the underlying bony toothplate fails

prior to the tooth, which leads to the "detachment" of the failed tooth and exposes the new tooth underneath (assuming the new tooth is ready to become functional), facilitating the subsequent replacement process.

Post-mortem SEM imaging again reveals the twisted and rough fracture in the enameloid compared to the clean and planar fracture surface in dentin (**Fig. 8D,E**), consistent with their microstructures (**Fig. 3**). Besides, and extensive crack deflection was observed near DEJ, which is believed due to the sharp transition of the microstructures (**Fig. 8E**). The crack morphologies in 3D were further characterized through synchrotron μCT-based *in-situ* mechanical tests (**Fig. 8F-J** and Fig. S9). **Fig. 8F** shows a projection of a tooth sample under compression, where the crack transects the entire thickness. Corresponding 3D rendering of the crack shows similar fracture morphologies observed in post-mortem SEM imaging, *i.e.*, corrugated and rough crack surfaces in inner enameloid *vs*. planar cracks in dentin (**Fig. 8G**). Some micro-cracks, especially in the outer enameloid, are neglected during rendering due to the resolution limit; therefore, the connecting micro-cracks in the outer enameloid might form a more complex network than the presented 3D rendering.

Detailed correlation between the crack morphologies with tooth microstructures reveal several important toughening mechanisms. Firstly, the cracks in the enameloid start as straight paths near the biting surfaces which become decussated and deflected into the inner enameloid (**Fig. 8H**-i), correlating with the gradual variations of the enameloid microstructures (**Fig. 3E,F**). Secondly, in the enameloid, a high density of the microcracks reduces the stress intensity ahead of the crack tip, therefore inhibits crack propagation [64], while the meandering cracks diverge around the enameloid rods and generate torturous paths (**Fig. 8I**) [65]. Thirdly, some micro-cracks stopped before approaching to inner enameloid (**Fig. 8H**-ii), which indicates the effective crack impeding by the decussated microstructures of enameloid rods. Fourthly, upon entering dentin, crack surfaces follow the direction of dentin tubules and propagate straight into deeper dentin (**Fig. 8J**); the occasional tubule branching might contribute to crack deflection into the horizontal direction (**Fig. 8H**-iii). In addition, layered oscillations were observed in the inner dentin (Fig. S10K); while the structural origin is still under investigation, the mechanical contribution of the oscillated dentin tubules might contribute to crack deflection and thus impede crack penetration across the dentin thickness. Finally, the density of dentin tubules is about an order of magnitude larger than tooth dentin in many animals (*e.g.*, human, alligators/crocodiles, dinosaurs, *etc.*), while another durophagous fish, sheephead (*Archosargus probatocephalus*), also has comparable dentin tubule density ($0.65 - 1.15 \times 10^5$ per mm^2) [66]. The density of dentin tubules might correlate with the functional requirements of tooth structures; for instance, herbivorous species of dinosaurs have a higher density of dentin tubules than carnivores [35]. Therefore, the higher dentin tubule density in durophagous fish might contribute to the enhanced energy dissipation by accommodating more deformation. Additional *in-situ* tests, including compression and wedge-tip indentation, were conducted on samples with epoxy-fixed bottom periphery (Fig. S9), which revealed similar cracking behaviors as that in the unfixed samples.

3.7. Macroscopic mechanical behavior: computational analysis

We next combined the structural, mechanical, and geometrical analysis results discussed above with systematic FE simulations to further investigate the stress/strain distribution within the enameloid-dentin-bone composite architecture under compressive loadings (Supplementary note 5). Axisymmetric 3D models were generated based on the representative structure of mature teeth, where the interfaces of DEJ and the dentin-bone junction were simplified as perfect bonding (**Fig. 9A** and Fig. S10). In order to evaluate the effects of the underlying bony toothplate, all simulations were conducted under two different setups, *i.e.*, with/without the bony toothplate (**Fig. 9B,C**). Directions 1,2, and 3 represent the radial,

vertical, and circumferential directions, respectively. In the simulations, the enameloid, dentin, and bone were all simplified as isotropic and elastic-perfectly plastic materials, while the target loads used for FE study were 200 and 400 N (representing loads for elastic deformation and failure, respectively, see Fig. S8). Although the top surface of some mature teeth is occasionally concave featured with a centered shallow crater, our FE analysis reveals that the topology of the top surface does not have significant effects on the stress distribution in the tooth models (Fig. S11). Hence, our following analysis is based on the models with an almost flat top surface (very shallow centered crater). It must be noted that the FE simulations here was used primarily to investigate the stress-strain distributions to correlate with fracture behavior observed in compression experiences. The extracted stress-strain values may deviate from actual values due to the simplification in the material models, such as mechanical anisotropy, internal mechanical property gradient, and length-scale dependence of mechanical properties of enameloid and dentin [67–69].

Considering the observed brittle fracture of teeth under compression, the maximum principal stress (σ_{max}) was taken as the primary failure criterion (**Fig. 9B,C**). The detailed stress contours (including σ_{max}, normal stresses σ_{11}, σ_{22}, σ_{33}, shear stress σ_{12}, and von Mises stress σ_{von}) and strain contours (including normal strains ε_{11}, ε_{22}, ε_{33}, and shear strain ε_{12}) are included in Figs. S12 and S13 for compression loads of 200 N and 400 N, respectively. The σ_{max} contours in both models with/without the bony toothplate show that compression induces an in-plane compressive stress field in the outer enameloid under direct contact (**Fig. 9b**-i and Fig. S12). Besides, tensile stress concentration is observed in the inner enameloid close to DEJ, and the sharp contrast of stress across the DEJ interface results from the property mismatch (**Fig. 9b**-ii). Interestingly, there is a higher tensile stress field at the thinnest thickness of enameloid (**Fig. 9b**-iii), which originates from the σ_{33}, normal stress along the circumferential direction (Fig. S12D). The inner dentin exhibits a tensile stress field, as the compression load induces a bending-like deformation (**Fig. 9B**-iv). Under higher loads (400 N), the stress contours are quite similar but with expanded regions and elevated stress levels (**Fig. 9C** and Fig. S13). In addition, a higher tensile stress σ_{33} is found along the circumferential/hoop direction at the outer surface of dentin and enameloid (along the 1-2 plane, *i.e.*, vertical-radial plane, Fig. S14D), which may result in the experimentally observed vertical cracks (**Fig. 8C**-I). The failure load estimations are also comparable with experimental results, where FE simulations predict bone failure below 400 N and dentin failure under *ca.* 650 N (Supplementary note 5).

In terms of the effects of the underlying bony toothplate, the two models (with/without bony toothplate) revealed similar stress contours in the enameloid and dentin at lower loads (**Fig. 9B**). Under higher loads, however, the expanded region of higher tensile stress was noticed in dentin for the without-bone model (**Fig. 9C** and Fig. S13). In other words, by introducing the relatively softer bone, tensile stress concentration in the lower part of the dentin is significantly reduced. In the with-bone model, an enlarged region of compressive stress is located near the dentin-bone junction, inducing a triaxial compressive field and possible subsequent failure initiation in the foam-like toothplate (Fig. S13B-D). In addition, the fibrous organics at the dentin-bone interface facilitate the deformation. As shown in Fig. S13G, large tensile strain ε_{11} is found close to the interface between dentin and bone, while the organic fibers at this interface are clearly beneficial in resisting the premature tensile strain-induced failure [33]. On the other hand, the solid contact between the dentin and bone in the contact rim helps to resist compressive strain ε_{22} (Fig. S13H).

Another interesting perspective of black drum teeth is the enlarged pulp chamber compared to teeth from other animals. An artificial model with a dentin-filled pulp chamber was generated for comparison, where the stress in the dentin is significantly reduced (Figs. S14 and S15). However, there is no

noticeable decrease in the normal stresses and strains in the bone component (Figs. S14A-C, and S15A-C), and increases in the shear stress and strain were observed (Figs. S14D,E and S15D,E). Since the bone is the weakest component in the composite, filling up the chamber increases the shear stress level in the bone, which reduces the load-bearing capacity of the teeth-bone composite. Thereby, the large size of the pulp chamber may contribute to reducing the effective stiffness of the "dentin component" at the structural level, which in turn reduces the maximum stress in the "bone component" by accommodating more deformation in the chambered dentin. This balanced stiffness by intrinsic properties and structural design between different components promotes beneficial stress distribution and improves the maximum biting force of the teeth. In live animals, the presence of fluid in the pulp chamber and dentin tubules might contribute to impact mitigation as well, further experimental and computational analysis are required to reveal the detailed mechanisms of the solid-fluid interaction between dentin (tubules) and pulp.

4. Discussion

The black drum fish teeth, similar to teeth in many organisms, are characterized by the classic two-layered enameloid-dentin design. The durophagous behavior, however, requires black drum fish teeth to have damage resistance at material level (near tooth surface), crack impediment across the DEJ, and structurally stiffness and controlled failure at the tooth-bone composite level under high crushing forces.

4.1. Design strategies at the material level

The combined microstructural, crystallographic, chemical, and mechanical characterizations reveal that the black drum teeth enameloid utilizes highly specialized material-level design strategies in the outer enameloid to avoid brittle fracture during tooth-shell contact.

The outer enameloid surface exhibits the highest modulus among the reported highly mineralized biological materials, which is attributed to concentrated Zn- and F-doping, as well as the preferential co-alignment of the *c*-axes of apatite crystals and enameloid rods with the biting direction. It is known that incorporation of F stiffens and hardens the HA crystal, considering that FA crystals have higher stiffness constants [54,70], bulk moduli [71], and hardness [51] compared to HA crystals. In black drum fish enameloid, F-doping may contribute to the increased indentation properties ($H = 5.0 \pm 1.4$ GPa, $E_r = 126.9 \pm 16.3$ GPa, F concentration of 2.65 *at.%* in Table S5) in comparison to human tooth enamel ($H = 3.5 - 4.8$ GPa, $E_r = 75 - 90$ GPa) [72,73], where the F concentration was found to be <0.2 *at.%* [74]. Regarding the toughening contribution of F-doping in HA crystals, even though single crystal FA has lower fracture toughness than HA single crystal [59,60], recent nanoindentation studies reported that powder-sintered (polycrystalline) fluoridated HA discs showed increasing toughness with the increase of fluoridation [49,50]. Interestingly, an early study on the teeth of 78 perciform fish species revealed that nearly all species have > 2.0% fluoride, regardless of their habitats (freshwater or marine) or the morphological adaptation of the teeth [75]. F-doping has also been found in many other biominerals, such as the stomatopod dactyl clubs and spears [63]. Based on a general comparison, the aqueous species have higher F concentration in the apatite, indicating additional correlation with the biological functionalities. In fact, it has long been recognized that F-substitution significantly decreases the solubility of HAP, which is essential for the durability of the apatite-based minerals in aqueous species [76,77]. Unlike F-doping, the incorporation of Zn as a cationic trace element in HA/FA crystals is less observed in fish teeth. However, Zn incorporation in the incisors of a freshwater prawn (*Macrobrachium rosenbergii*) was shown to enhance its hardness in a recent report [78]. Similar correlation between the local Zn

concentration and properties was also reported in the toothed jaws of a marine worm, *Nereis limbata* [79]. A previous modeling-based investigation suggests that the Zn substitution in HA crystals can lead to improved mechanical properties (modulus, hardness, and toughness) with the optimal concentration of $n_{Zn}/n_{(Zn+Ca)}$ < 2.5 *at.%* (atomic percentage) [55]. In black drum teeth, the average Zn concentration in enameloid is within the optimal range (1.9 *at.%*, Table S5), although further investigation is required to understand the spatial distribution of Zn substitution at individual crystal level.

The co-alignment of the enameloid rods and the apatite *c*-axes near the tooth surface revealed by PIC mapping may contribute to the enhanced crack resistance on the tooth surface, since shorter indentation cracks were measured on the basal plane (loaded along the *c*-axis) of FA crystals compared to the side planes [51]. This indicates that the advantage of the alignment of the crystal *c*-axis along the biting direction might involve better crack resistance under contact. Moreover, the modulus ratio of the outer enameloid along and across the biting direction is 1.17, close to the modulus ratio parallel and perpendicular to the *c*-axis in FA crystal [53]. This further supports that the HA/FA crystallites orient their stiffer *c*-axis preferably along the biting direction, and similar structural control has been observed in the teeth of other durophagous fish, such as the black carp (*M. piceus*), where the preferential *c*-axis alignment of the apatite crystals is reported to enhance the wear resistance [37,80].

The micro-structural and chemical designs were combined to enhance the stiffness and toughness near the tooth surface for improved performance against tooth-shell contact when crushing mollusk shells during feeding. To characterize the damage mode during contact, brittle index I_B can be used to determine whether the black drum teeth experience quasi-plastic yielding (I_B < 1) or brittle fracture (I_B > 1),

$$I_B = \frac{P_{yielding}}{P_{cracking}} = \left(\frac{D}{A}\right)\left(\frac{H}{E_{eff}}\right)\left(\frac{H}{K_c}\right)^2 R_{eff} \tag{4},$$

where $P_{yielding}$ and $P_{cracking}$ are the critical external loads to initiate yielding or cracking; $D = 0.85$ and $A = 8.6 \times 10^3$ are constant coefficients for quasi-plastic mode and fracture mode, respectively; E_{eff} and R_{eff} are the effective modulus and effective radius depending on the materials and geometries of two materials during contact (Supplementary note 6) [81]. The concept of brittle index I_B was originally used to determine the damage mode (brittle *vs.* quasi-plastic) of ceramics under Hertzian contact [81], which was later introduced to predict the damage in hard biominerals as well, including parrotfish teeth against hard coral [36], and contact damage of stomatopod dactyl clubs [82]. Based on the I_B maps for tooth-shell contact, the black drum tooth enameloid is estimated to experience plastic yielding at local scale around the contact point when the mollusk shells are properly positioned in the masticatory apparatus (Supplementary note 6). The mollusks usually have thin shell thickness, which further facilitates the crushability of the shells during tooth-shell contact [37]. The shell debris found in the digestive tract of the black drum fish also confirmed the brittle fracture of mollusk shells [12].

4.2. Design strategies at individual tooth level

At the individual tooth level, the unique tooth geometry, the classic two-layered enameloid-dentin design, and the strong underlying bony toothplate allow the black drum teeth to sustain extremely high compressive loads (up to 150-600 N for isolated teeth). The overall geometrical characteristics of the individual teeth can be summarized as following major points: molariform teeth, smooth top surface, cylindrical geometry with a typical thickness of 1-2 mm (enameloid thickness *ca.* 1/3 of the entire tooth thickness), and absence of deep dentin root. The tooth morphologies are closely related to the functional requirements.

(1) The molariform teeth with smooth enameloid surface adapt to the crushing-dominated feeding behaviors. Compared with fish teeth adapted to other feeding styles, *e.g.*, sharp canine-like teeth in the Amazon dogfish (*Rhaphiodon vulpinus*) used to puncture and hold prey and sharp triangular teeth with serrated cutting edge adapted to slicing and sawing prey in piranha (*Serrasalmus manueli*) and the great white shark (*Carcharodon carcharias*) [83,84], the molariform teeth are designed to withstand compressive crushing force perpendicular to the tooth surface. During mollusk crushing, triaxial compression is concentrated at the contact point due to the surface curvatures on the teeth and shell surfaces, which helps localize the damage. At the local scale, the much smaller surface radii of teeth compared to mollusk shells enables that plastic yielding predominates during tooth-shell contact. Even if the crack initiates under extreme contact, the downwards crushing force induces the bending deformation of the tooth, and the compressive stress field in the enameloid region may constrain crack formation on the surface.

(2) The sharp property contrast across the DEJ interface induces the large mismatch of the in-plane shear stress and strain (**Fig. 6A,B**, Figs.S13E,J and S14E,J). However, the interlaced microstructures near the DEJ form the interdigitating interfaces between dentin and enameloid (**Fig. 3A**), which interrupt the stress field and help avoid interfacial failure.

(3) Regarding the dentin design, the interior surface resists in-plane tension, while the surrounding dentin help withstand compression. Similar to other teeth systems, dentin is designed to be softer and compliant for more energy absorption. The significantly higher density of dentin tubules in durophagous, including both the black drum (**Fig. 3B,C**) and sheephead fish [66], might contribute to higher energy-absorption capacity in durophagous fish. While the dentin-bone junction design (**Fig. 2D,E** and Fig. S3) also facilitates the strains under high compressive loads, specifically, compressive strain below the surrounding dentin by the contact rim (ε_{22} in Fig. S13H) and tensile strains both along the loading and lateral direction by the fibrous organics (ε_{11} in Fig. S13G and ε_{22} in Fig. S13H).

(4) In addition, the black drum teeth have enlarged chamber and cavity below (estimated volume ratios, $V_{pulp}/V_{teeth} = 0.20$, $V_{pulp+cavity}/V_{teeth} = 0.46$) compared to other teeth, including human, piranha [83], parrotfish [36], and shark teeth [51], *etc.* Our FE analysis shows that such an enlarged pulp chamber reduces the shear stress and strain in the bone (Figs. S15E and S16E). Since bone is the weakest component in the enameloid-dentin-bone composite, it is likely that the enlarged pulp chamber avoids premature failure in the bone, and thus enhances the load capacity of the composite.

4.3. Design strategies at tooth-bone composite level

At the level of the pharyngeal jaw, the teeth assembly aligns the larger teeth towards the central region on the toothplate for higher resistance against crushing loads, in comparison to the line arrangements of human molar teeth, which mainly function for grinding and tearing (Fig. S2). Another feature to notice is that the tooth crowns (enameloid surfaces) have different shapes at different locations, which might be designed for specific purposes: the pointy teeth at the peripheries of the pharyngeal jaws may be used for retaining the soft tissue of mollusks when ejecting shell fragments out after shell breakage (Fig. S3).

Finally, the foam-like bony structure in the toothplate represents an energy absorber under crushing loads (**Fig. 8A,B**). Additionally, being the weakest component of the pharyngeal teeth, the bony toothplate undergoes failure first under excessive loads, leading to detachment of failed tooth from the toothplate. With the cavity below the functioning teeth, the newly formed teeth in the toothplate can erupt

and replace the failed one easily. Compared with human permanent teeth, the black drum teeth do not have deep roots embedded in bony tissue, further facilitating the replacement of the failed teeth.

5. Conclusion

In conclusion, the tooth design of black drum fish is an effective adaptation for its molluscivorous feeding behavior. The efficient design is achieved through multiscale control, including (1) microstructural and chemical gradients at the microscopic level of the outer enameloid, (2) molariform surface geometry, interdigitated DEJ interface, high density of dentin tubules, and enlarged pulp chamber at the entire tooth level, and (3) foam-like toothplates at the level of pharyngeal jaw. The chemical doping and crystallographic alignment near the tooth surface enables superior stiffness, hardness, and fracture resistance, promoting quasi-plastic yielding as the preferable deformation mode of teeth when in contact with mollusks shells. With molariform tooth surface constraining compressive stress in stiff enameloid, interwoven DEJ avoiding interfacial failure, dentin tubules for energy absorption, and enlarged pulp chamber preventing premature failure in the bone, the different design strategies at the individual tooth level are adapted to the crushing-dominated feeding behaviors of the black drum teeth. Under extreme loadings, the weak toothplates induce failure of the teeth-bone connection and detachment of failed teeth, which allow easy tooth replacement and eruption. The study of the black drum teeth can potentially provide inspirations for bioinspired designs across multiple scales, including the material and structural levels for integrated functionality.

Declaration of Competing Interest

The authors declare no conflict of interest.

Acknowledgements

Author contributions

L.L. supervised the research. Z.D. conducted the mechanical experiments and tomographic measurements (nanoindentation and fracture toughness measurements, X-ray tomography and in-situ mechanical testing, macroscopic mechanical testing, and electron microscopy). H.C.L. and A.M. performed chemical characterizations (Raman spectroscopy and energy dispersive X-ray spectroscopy). Z.J. performed finite element analysis. C.A.S. and P.G. performed crystallographic characterizations (Polarization-dependent imaging contrast mapping). Z.D. and L.L. analyzed the data and wrote the draft manuscript. All authors contributed to data interpretation and manuscript preparation.

References

[1] W. Yang, H. Quan, M.A. Meyers, R.O. Ritchie, Arapaima Fish Scale: One of the Toughest Flexible Biological Materials, Matter. 1 (2019) 1557–1566. https://doi.org/10.1016/j.matt.2019.09.014.

[2] J. Wang, M. Tenjimbayashi, Y. Tokura, J.Y. Park, K. Kawase, J. Li, S. Shiratori, Bionic Fish-Scale Surface Structures Fabricated via Air/Water Interface for Flexible and Ultrasensitive Pressure Sensors, ACS Appl. Mater. Interfaces. 10 (2018) 30689–30697. https://doi.org/10.1021/acsami.8b08933.

[3] M. Kreysin, R. Pusch, D. Haverkate, M. Landsberger, J. Engelmann, J. Ruiter, C. Mora-Ferrer, E. Ulbricht, J. Grosche, K. Franze, S. Streif, S. Schumacher, F. Makarov, J. Kacza, J. Guck, H. Wolburg, J.K. Bowmaker, G. von der Emde, S. Schuster, H.-J. Wagner, A. Reichenbach, M. Francke, Photonic Crystal Light Collectors in Fish Retina Improve Vision in Turbid Water, Science. 336 (2012) 1700–1703.

[4] A. Raj, A. Thakur, Fish-inspired robots: design, sensing, actuation, and autonomy—a review of research, Bioinspir. Biomim. 11 (2016) 031001.

[5] S.E. Naleway, J.R.A. Taylor, M.M. Porter, M.A. Meyers, J. McKittrick, Structure and mechanical properties of selected protective systems in marine organisms, Mater. Sci. Eng. C. Mater. Biol. Appl. 59 (2016) 1143–67. https://doi.org/10.1016/j.msec.2015.10.033.

[6] B. Bhushan, Biomimetics: lessons from nature-an overview, Philos. Trans. R. Soc. A Math. Phys. Eng. Sci. 367 (2009) 1445–1486. https://doi.org/10.1098/rsta.2009.0011.

[7] D.W. Bechert, M. Bruse, W. Hage, R. Meyer, Fluid mechanics of biological surfaces and their technological application, Naturwissenschaften. 87 (2000) 157–171. https://doi.org/10.1007/s001140050696.

[8] J.R. Grubich, Crushing motor patterns in drum (Teleostei: Sciaenidae): Functional novelties associated with molluscivory, J. Exp. Biol. 203 (2000) 3161–3176.

[9] C.D. Wilga, P.J. Motta, Durophagy in sharks: feeding mechanics of the hammerhead Sphyrna tiburo, J. Exp. Biol. 203 (2000) 2781–2796.

[10] P. Vandewalle, É. Parmentier, M. Chardon, The branchial basket in teleost feeding, Cybium. 24 (2000) 319–342.

[11] E. Ziv, J. Milgram, J. Davis, A. Soares, F. Wilde, P. Zaslansky, R. Shahar, Neither cortical nor trabecular: An unusual type of bone in the heavy-load-bearing lower pharyngeal jaw of the black drum (Pogonias cromis), Acta Biomater. 104 (2020) 28–38. https://doi.org/10.1016/j.actbio.2020.01.001.

[12] A.S. Cate, I. Evans, Taphonomic Significance of the Biomechanical Fragmentation of Live Molluscan Shell Material by a Bottom-Feeding Fish (Pogonias cromis) in Texas Coastal Bays, Palaios. 9 (1994) 254–274. https://doi.org/10.2307/3515201.

[13] J.R. Grubich, Disparity between feeding performance and predicted muscle strength in the pharyngeal musculature of black drum, Pogonias cromis (Sciaenidae), Environ. Biol. Fishes. 74 (2005) 261–272. https://doi.org/10.1007/s10641-005-3218-0.

[14] J. Grubich, Morphological convergence of pharyngeal jaw structure in durophagous perciform fish, Biol. J. Linn. Soc. 80 (2003) 147–165. https://doi.org/10.1046/j.1095-8312.2003.00231.x.

[15] S. Wroe, C. McHenry, J. Thomason, Bite club: Comparative bite force in big biting mammals and the prediction of predatory behaviour in fossil taxa, Proc. R. Soc. B Biol. Sci. 272 (2005) 619–625. https://doi.org/10.1098/rspb.2004.2986.

[16] J.R. Grubich, S. Huskey, S. Crofts, G. Orti, J. Porto, Mega-Bites: Extreme jaw forces of living and extinct piranhas (Serrasalmidae), Sci. Rep. 2 (2012) 1–9. https://doi.org/10.1038/srep01009.

[17] N.J. Hite, C. Germain, B.W. Cain, M. Sheldon, S.S.N. Perala, D.K. Sarko, The Better to Eat You With: Bite Force in the Naked Mole-Rat (Heterocephalus glaber) Is Stronger Than Predicted Based on Body Size, Front. Integr. Neurosci. 13 (2019) 1–14. https://doi.org/10.3389/fnint.2019.00070.

[18]   D.R. Huber, M.N. Dean, A.P. Summers, Hard prey, soft jaws and the ontogeny of feeding mechanics in the spotted ratfish Hydrolagus colliei, J. R. Soc. Interface. 5 (2008) 941–952. https://doi.org/10.1098/rsif.2007.1325.

[19]   D.R. Huber, T.G. Eason, R.E. Hueter, P.J. Motta, Analysis of the bite force and mechanical design of the feeding mechanism of the durophagous horn shark Heterodontus francisci, J. Exp. Biol. 208 (2005) 3553–3571. https://doi.org/10.1242/jeb.01816.

[20]   G. De Stasio, B.H. Frazer, B. Gilbert, K.L. Richter, J.W. Valley, Compensation of charging in X-PEEM : a successful test on mineral inclusions in 4 . 4 Ga old zircon, Ultramicroscopy. 98 (2003) 57–62. https://doi.org/10.1016/S0304-3991(03)00088-3.

[21]   R.T. Devol, R.A. Metzler, L. Kabalah-amitai, B. Pokroy, Y. Politi, A. Gal, L. Addadi, S. Weiner, A. Fernandez-martinez, J.D. Gale, J. Ihli, F.C. Meldrum, A.Z. Blonsky, C.E. Killian, C.B. Salling, A.T. Young, M.A. Marcus, A. Scholl, A. Doran, C. Jenkins, H.A. Bechtel, P.U.P.A. Gilbert, Oxygen Spectroscopy and Polarization-Dependent Imaging Contrast (PIC)-Mapping of Calcium Carbonate Minerals and Biominerals, J. Phys. Chem. B. 118 (2014) 8449–8457.

[22]   R.A. Metzler, M. Abrecht, R.M. Olabisi, D. Ariosa, C.J. Johnson, B.H. Frazer, S.N. Coppersmith, P.U.P.A. Gilbert, Architecture of columnar nacre, and implications for its formation Mechanism, Phys. Rev. Lett. 98 (2007) 1–4. https://doi.org/10.1103/PhysRevLett.98.268102.

[23]   R.A. Metzler, D. Zhou, M. Abrecht, J. Chiou, J. Guo, D. Ariosa, S.N. Coppersmith, P.U.P.A. Gilbert, Polarization-dependent imaging contrast in abalone shells, Phys. Rev. B. 77 (2008) 064110. https://doi.org/10.1103/PhysRevB.77.064110.

[24]   P.U.P.A. Gilbert, A. Young, S.N. Coppersmith, Measurement of c-axis angular orientation in calcite (CaCO 3) nanocrystals using X-ray absorption spectroscopy, Proc. Natl. Acad. Sci. U. S. A. 108 (2011) 11350–11355. https://doi.org/10.1073/pnas.1107917108.

[25]   B. Gilbert, R. Andres, P. Perfetti, G. Margaritondo, G. Rempfer, G. De Stasio, Charging phenomena in PEEM imaging and spectroscopy, Ultramicroscopy. 83 (2000) 129–139.

[26]   T. Parasassi, O. Sapora, A. Giusti, G. De Stasio, G. Ravagnan, Alterations in erythrocyte membrane lipids induced by low doses of ionizing radiation as revealed by 1, 6-diphenyl-1, 3, 5-hexatriene fluorescence lifetime, Int. J. Radiat. Biol. 59 (1991) 59–69.

[27]   C.A. Stifler, N.K. Wittig, M. Sassi, C. Sun, M.A. Marcus, H. Birkedal, E. Beniash, K.M. Rosso, P.U.P.A. Gilbert, X - ray Linear Dichroism in Apatite, J. Am. Chem. Soc. 140 (2018) 11698–11704. https://doi.org/10.1021/jacs.8b05547.

[28]   W.C. Oliver, G.M. Pharr, An improved technique for determining hardness and elastic modulus using load and displacement sensing indentation experiments, J. Mater. Res. 7 (1992) 1564–1583. https://doi.org/10.1557/JMR.1992.1564.

[29]   D. Gürsoy, F. De Carlo, X. Xiao, C. Jacobsen, TomoPy: A framework for the analysis of synchrotron tomographic data, J. Synchrotron Radiat. 21 (2014) 1188–1193. https://doi.org/10.1107/S1600577514013939.

[30]   Y.T. Cheng, C.M. Cheng, Scaling approach to conical indentation in elastic-plastic solids with work hardening, J. Appl. Phys. 84 (1998) 1284–1291. https://doi.org/10.1063/1.368196.

[31]   E.A. Zimmermann, E. Schaible, H. Bale, H.D. Barth, S.Y. Tang, P. Reichert, B. Busse, T. Alliston, J.W. Ager, R.O. Ritchie, Age-related changes in the plasticity and toughness of human cortical bone at multiple length scales, Proc. Natl. Acad. Sci. 108 (2011) 14416–14421. https://doi.org/10.1073/pnas.1107966108.

[32]   B.J.F. Bruet, J. Song, M.C. Boyce, C. Ortiz, Materials design principles of ancient fish armour, Nat. Mater. 7 (2008) 748–756. https://doi.org/10.1038/nmat2231.

[33]   E. Raguin, K. Rechav, V. Brumfeld, R. Shahar, S. Weiner, Unique three-dimensional structure of a fish mandible bone subjected to unusually high mechanical loads, J. Struct. Biol. 211 (2020) 107530. https://doi.org/10.1016/j.jsb.2020.107530.

[34]   T. Komabayashi, G. Nonomura, L.G. Watanabe, G.W. Marshall, S.J. Marshall, Dentin tubule numerical density variations below the CEJ, J. Dent. 36 (2008) 953–958. https://doi.org/10.1016/j.jdent.2008.08.002.Dentin.

[35] K.S. Brink, Y.C. Chen, Y.N. Wu, W.M. Liu, D. Bin Shieh, T.D. Huang, C.K. Sun, R.R. Reisz, Dietary adaptions in the ultrastructure of dinosaur dentine, J. R. Soc. Interface. 13 (2016). https://doi.org/10.1098/rsif.2016.0626.

[36] M.A. Marcus, S. Amini, C.A. Stifler, C.Y. Sun, N. Tamura, H.A. Bechtel, D.Y. Parkinson, H.S. Barnard, X.X.X. Zhang, J.Q.I. Chua, A. Miserez, P.U.P.A. Gilbert, Parrotfish Teeth: Stiff Biominerals Whose Microstructure Makes Them Tough and Abrasion-Resistant to Bite Stony Corals, ACS Nano. 11 (2017) 11856–11865. https://doi.org/10.1021/acsnano.7b05044.

[37] C. He, W. Zhou, H. Wang, S.Q. Shi, H. Yao, Mechanics of pharyngeal teeth of black carp (mylopharyngodon piceus) crushing mollusk shells, Adv. Eng. Mater. 15 (2013) 684–690. https://doi.org/10.1002/adem.201200304.

[38] M. Campillo, P.D. Lacharmoise, J.S. Reparaz, A.R. Goñi, M. Valiente, On the assessment of hydroxyapatite fluoridation by means of Raman scattering, J. Chem. Phys. 132 (2010). https://doi.org/10.1063/1.3428556.

[39] G. Gouadec, P. Colomban, Raman Spectroscopy of nanomaterials: How spectra relate to disorder, particle size and mechanical properties, Prog. Cryst. Growth Charact. Mater. 53 (2007) 1–56. https://doi.org/10.1016/j.pcrysgrow.2007.01.001.

[40] I. Notingher, Characterisation using Raman micro-spectroscopy, in: A.R. Boccaccini, J.E. Gough (Eds.), Tissue Eng. Using Ceram. Polym., Woodhead Publishing Series in Biomaterials, 2007: pp. 248–266. https://www.sciencedirect.com/science/article/pii/B9781845691769500125.

[41] J. Kong, S. Yu, Fourier transform infrared spectroscopic analysis of protein secondary structures, Acta Biochim. Biophys. Sin. (Shanghai). 39 (2007) 549–559. https://doi.org/10.1111/j.1745-7270.2007.00320.x.

[42] F.N. Fu, D.B. DeOliveira, W.R. Trumble, H.K. Sarkar, B.R. Singh, Secondary structure estimation of proteins using the amide III region of fourier transform infrared spectroscopy: application to analyze calcium-binding-induced structural changes in calsequestrin, Appl. Spectrosc. 48 (1994) 1432–1441. https://doi.org/10.1366/0003702944028065.

[43] G.W. Marshall, S.J. Marshall, J.H. Kinney, M. Balooch, The dentin substrate: structure and properties related to bonding, J. Dent. 25 (1997) 441–458.

[44] V. Imbeni, R.K. Nalla, C. Bosi, J.H. Kinney, R.O. Ritchie, In vitro fracture toughness of human dentin, J. Biomed. Mater. Res. - Part A. 66 (2003) 1–9. https://doi.org/10.1002/jbm.a.10548.

[45] R.K. Nalla, J.H. Kinney, R.O. Ritchie, Effect of orientation on the in vitro fracture toughness of dentin: The role of toughening mechanisms, Biomaterials. 24 (2003) 3955–3968. https://doi.org/10.1016/S0142-9612(03)00278-3.

[46] S. Sprio, G. Pezzotti, G. Celotti, E. Landi, A. Tampieri, Raman and cathodoluminescence spectroscopies of magnesium-substituted hydroxyapatite powders, J. Mater. Res. 20 (2005) 1009–1016. https://doi.org/10.1557/JMR.2005.0132.

[47] E. Beniash, C.A. Stifler, C.Y. Sun, G.S. Jung, Z. Qin, M.J. Buehler, P.U.P.A. Gilbert, The hidden structure of human enamel, Nat. Commun. 10 (2019) 1–13. https://doi.org/10.1038/s41467-019-12185-7.

[48] C.A. Stifler, J.E. Jakes, J.D. North, D.R. Green, J.C. Weaver, P.U.P.A. Gilbert, Crystal misorientation correlates with hardness in tooth enamels, Acta Biomater. 120 (2021) 124–134. https://doi.org/10.1016/j.actbio.2020.07.037.

[49] K.A. Gross, K.A. Bhadang, Sintered hydroxyfluorapatites. Part III: Sintering and resultant mechanical properties of sintered blends of hydroxyapatite and fluorapatite, Biomaterials. 25 (2004) 1395–1405. https://doi.org/10.1016/j.biomaterials.2003.08.051.

[50] H. Eslami, M. Solati-Hashjin, M. Tahriri, The comparison of powder characteristics and physicochemical, mechanical and biological properties between nanostructure ceramics of hydroxyapatite and fluoridated hydroxyapatite, Mater. Sci. Eng. C. 29 (2009) 1387–1398. https://doi.org/10.1016/j.msec.2008.10.033.

[51] J. Enax, O. Prymak, D. Raabe, M. Epple, Structure, composition, and mechanical properties of shark teeth, 178 (2012) 290–299.

[52]   S. Amini, A. Miserez, Wear and abrasion resistance selection maps of biological materials, Acta Biomater. 9 (2013) 7895–7907. https://doi.org/10.1016/j.actbio.2013.04.042.

[53]   D. Mkhonto, N.H. de Leeuw, A computer modelling study of the effect of water on the surface structure and morphology of fluorapatite: Introducing a Ca10(PO4)6F2 potential model, J. Mater. Chem. 12 (2002) 2633–2642. https://doi.org/10.1039/b204111a.

[54]   E. Menéndez-proupin, S. Cervantes-rodríguez, R. Osorio-pulgar, M. Franco-cisterna, Computer simulation of elastic constants of hydroxyapatite and fluorapatite, J. Mech. Behav. Biomed. Mater. 4 (2011) 1011–1020. https://doi.org/10.1016/j.jmbbm.2011.03.001.

[55]   S. Aryal, K. Matsunaga, W. Ching, Ab initio simulation of elastic and mechanical properties of Zn- and Mg-doped hydroxyapatite (HAP), J. Mech. Behav. Biomed. Mater. 47 (2015) 135–146. https://doi.org/10.1016/j.jmbbm.2015.03.018.

[56]   A. Miserez, J.C. Weaver, P.J. Thurner, J. Aizenberg, Y. Dauphin, P. Fratzl, D.E. Morse, F.W. Zok, Effects of laminate architecture on fracture resistance of sponge biosilica: Lessons from nature, Adv. Funct. Mater. 18 (2008) 1241–1248. https://doi.org/10.1002/adfm.200701135.

[57]   G.M. Pharr, Measurement of mechanical properties by ultra-low load indentation, Mater. Sci. Eng. A. 253 (1998) 151–159. https://doi.org/10.1016/s0921-5093(98)00724-2.

[58]   G.R. Anstis, P. Chantikul, B.R. Lawn, D.B. Marshall, A Critical Evaluation of Indentation Techniques for Measuring Fracture Toughness: I, Direct Crack Measurements, J. Am. Ceram. Soc. 46 (1981) 533–538.

[59]   M.E. Broz, R.F. Cook, D.L. Whitney, Microhardness, toughness, and modulus of Mohs scale minerals, Am. Mineral. 91 (2006) 135–142. https://doi.org/10.2138/am.2006.1844.

[60]   I. Hervas, A. Montagne, A. Van Gorp, M. Bentoumi, A. Thuault, A. Iost, Fracture toughness of glasses and hydroxyapatite: A comparative study of 7 methods by using Vickers indenter, Ceram. Int. 42 (2016) 12740–12750. https://doi.org/10.1016/j.ceramint.2016.05.030.

[61]   M.A. Meyers, P.Y. Chen, A.Y.M. Lin, Y. Seki, Biological materials: Structure and mechanical properties, Prog. Mater. Sci. 53 (2008) 1–206. https://doi.org/10.1016/j.pmatsci.2007.05.002.

[62]   M. Yahyazadehfar, J. Ivancik, H. Majd, B. An, D. Zhang, D. Arola, On the Mechanics of Fatigue and Fracture in Teeth, Appl. Mech. Rev. 66 (2014) 0308031–3080319. https://doi.org/10.1115/1.4027431.

[63]   S. Amini, A. Masic, L. Bertinetti, J.S. Teguh, J.S. Herrin, X. Zhu, H. Su, A. Miserez, Textured fluorapatite bonded to calcium sulphate strengthen stomatopod raptorial appendages, Nat. Commun. 5 (2014) 1–12. https://doi.org/10.1038/ncomms4187.

[64]   M.E. Launey, R.O. Ritchie, On the fracture toughness of advanced materials, Adv. Mater. 21 (2009) 2103–2110. https://doi.org/10.1002/adma.200803322.

[65]   S. Bechtle, T. Fett, G. Rizzi, S. Habelitz, A. Klocke, G.A. Schneider, Crack arrest within teeth at the dentinoenamel junction caused by elastic modulus mismatch, Biomaterials. 31 (2010) 4238–4247. https://doi.org/10.1016/j.biomaterials.2010.01.127.

[66]   J.F. Deang, A.K. Persons, A.L. Oppedal, H. Rhee, R.D. Moser, M.F. Horstemeyer, Structure, property, and function of sheepshead (Archosargus probatocephalus) teeth, Arch. Oral Biol. 89 (2018) 1–8. https://doi.org/10.1016/j.archoralbio.2018.01.013.

[67]   S.F. Ang, E.L. Bortel, M. V. Swain, A. Klocke, G.A. Schneider, Size-dependent elastic/inelastic behavior of enamel over millimeter and nanometer length scales, Biomaterials. 31 (2010) 1955–1963. https://doi.org/10.1016/j.biomaterials.2009.11.045.

[68]   S. Bechtle, H. Özcoban, E.T. Lilleodden, N. Huber, A. Schreyer, M. V. Swain, G.A. Schneider, Hierarchical flexural strength of enamel: Transition from brittle to damage-tolerant behaviour, J. R. Soc. Interface. 9 (2012) 1265–1274. https://doi.org/10.1098/rsif.2011.0498.

[69]   S. Bechtle, S. Habelitz, A. Klocke, T. Fett, G.A. Schneider, The fracture behaviour of dental enamel, Biomaterials. 31 (2010) 375–384. https://doi.org/10.1016/j.biomaterials.2009.09.050.

[70]   T.N. Gardner, J.C. Elliott, Z. Sklar, G.A.D. Briggs, Acoustic microscope study of the elastic properties of fluorapatite and hydroxyapatite, tooth enamel and bone, J. Biomech. 25 (1992) 1265–1277.

[71] F. Brunet, D.R. Allan, S.A.T. Redfern, R.J. Angel, R. Miletich, H.J. Reichmann, J. Sergent, M. Hanfland, Compressibility and thermal expansivity of synthetic apatites, Ca5(PO4)3X with X = OH, F and Cl, Eur. J. Mineral. 11 (1999) 1023–1036. https://doi.org/10.1127/ejm/11/6/1023.

[72] S. Park, J.B. Quinn, E. Romberg, D. Arola, On the brittleness of enamel and selected dental materials, Dent. Mater. 24 (2008) 1477–1485. https://doi.org/10.1016/j.dental.2008.03.007.

[73] S. Habeliz, S.J. Marshall, G.W.M. Jr, M. Balooch, S. Habelitz, S.J. Marshall, G.W.M. Jr, M. Balooch, Mechanical properties of human dental enamel on the nanometre scale, Arch. Oral Biol. 46 (2001) 173–183. https://doi.org/10.1016/S0003-9969(00)00089-3.

[74] K.J. Scholz, M. Federlin, K.A. Hiller, H. Ebensberger, G. Ferstl, W. Buchalla, EDX-analysis of fluoride precipitation on human enamel, Sci. Rep. 9 (2019) 1–11. https://doi.org/10.1038/s41598-019-49742-5.

[75] S. Suga, Y. Taki, K. Wada, Fluoride Concentration in the Teeth of Perciform and Its Phylogenetic Significance, Japanese J. Ichthyol. 30 (1983) 81–93.

[76] T. Aoba, The effect of fluride on apatite structure and growth, Crit. Rev. Oral Biol. Med. 8 (1997) 136–153.

[77] K. Pajor, L. Pajchel, J. Kolmas, Hydroxyapatite and Fluorapatite in Conservative Dentistry and Oral Implantology—A Review, Materials (Basel). 12 (2019) 2683.

[78] S. Bentov, B.A. Palmer, B. Bar-On, Y. Shelef, E.D. Aflalo, A. Sagi, Reinforcement of bio-apatite by zinc substitution in the incisor tooth of a prawn, Acta Biomater. 120 (2021) 116–123. https://doi.org/10.1016/j.actbio.2020.07.039.

[79] J.T. Ruokolainen, J.O. Cross, S.M. Heald, H. Birkedal, H.C. Lichtenegger, T. Scho, J.H. Waite, G.D. Stucky, Zinc and mechanical prowess in the jaws of Nereis , a marine worm, Proc. Natl. Acad. Sci. U. S. A. 100 (2003).

[80] J. Fu, C. He, B. Xia, Y. Li, Q. Feng, Q. Yin, X. Shi, X. Feng, H. Wang, H. Yao, C-axis preferential orientation of hydroxyapatite accounts for the high wear resistance of the teeth of black carp (Mylopharyngodon piceus), Sci. Rep. 6 (2016) 1–9. https://doi.org/10.1038/srep23509.

[81] Y.W. Rhee, H.W. Kim, Y. Deng, B.R. Lawn, Brittle Fracture versus Quasi Plasticity in Ceramics: A Simple Predictive Index, J. Am. Ceram. Soc. 84 (2001) 561–565. https://doi.org/10.1111/j.1151-2916.2001.tb00698.x.

[82] S. Amini, M. Tadayon, S. Idapalapati, A. Miserez, The role of quasi-plasticity in the extreme contact damage tolerance of the stomatopod dactyl club, Nat. Mater. 14 (2015) 943–950. https://doi.org/10.1038/nmat4309.

[83] M.A. Meyers, Y.S. Lin, E.A. Olevsky, P.Y. Chen, Battle in the Amazon: Arapaima versus piranha, Adv. Eng. Mater. 14 (2012). https://doi.org/10.1002/adem.201180027.

[84] P.Y. Chen, A.Y.M. Lin, Y.S. Lin, Y. Seki, A.G. Stokes, J. Peyras, E.A. Olevsky, M.A. Meyers, J. McKittrick, Structure and mechanical properties of selected biological materials, J. Mech. Behav. Biomed. Mater. 1 (2008) 208–226. https://doi.org/10.1016/j.jmbbm.2008.02.003.

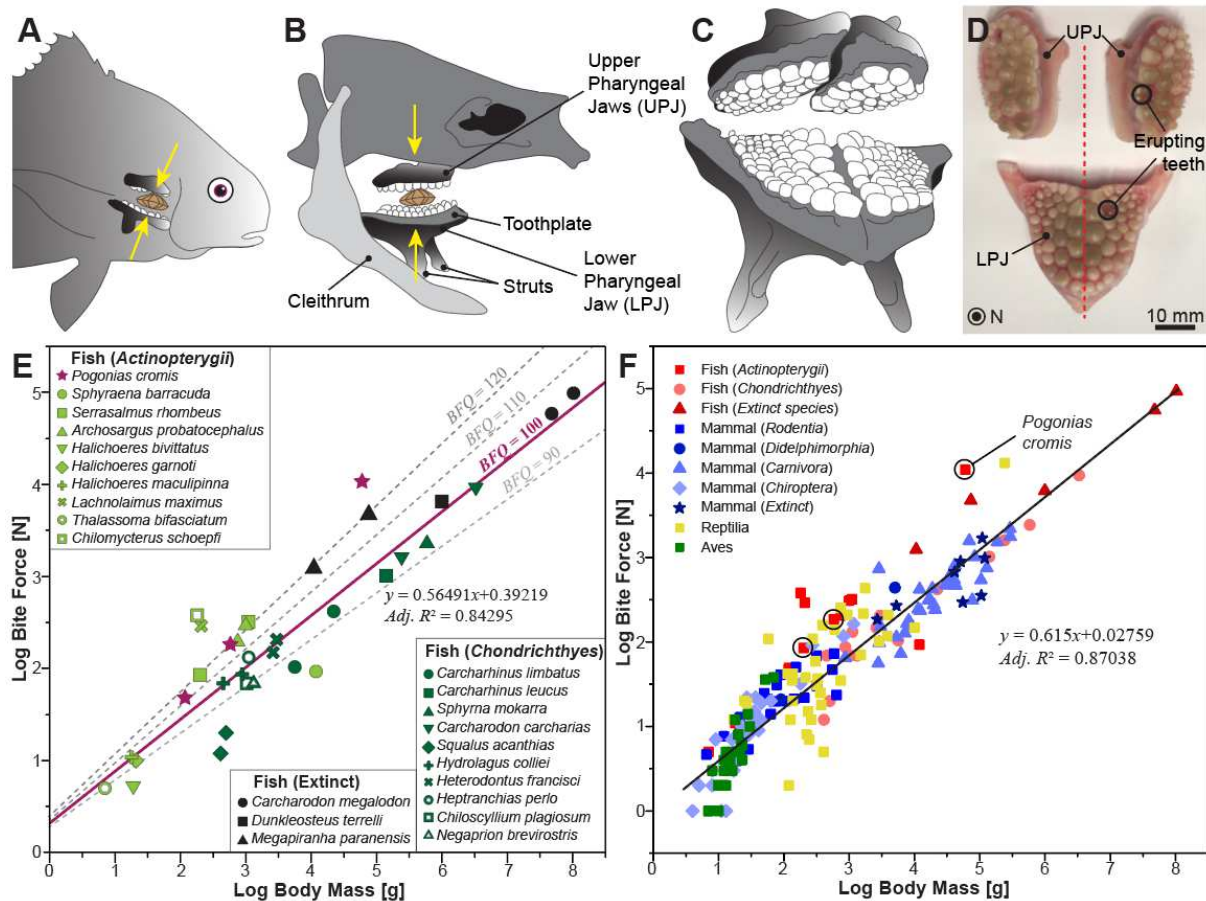# Figures and Tables

Figure 1 (full width)

Fig. 1. Pharyngeal jaws' performance in black drum fish (*P. cromis*). (A,B) Schematics of **(A)** location of the pharyngeal jaws in the throat of fish, and **(B)** crushing motor pattern, where the yellow arrows indicate simultaneous UPJ depression and LPJ elevation during crushing in black drum, and the red arrow indicates the UPJ retraction observed in non-molluscivorous fish, the red drum. **(C)** Schematic of a pair of pharyngeal jaws of black drum fish, including two upper pharyngeal jaws (UPJs) and lower pharyngeal jaw (LPJ). **(D)** Photo of a UPJs and LPJ showing the molariform teeth on the toothplates, where "N" denotes the normal (biting) direction. **(E)** Bite force quotients (*BFQ*) regression for different fish species, indicating that black drum fish has an advantageous mechanism for its masticatory apparatus. **(F)** *BFQ* regression for different vertebrate species, including fish, mammals, reptiles and birds, where the data points representing the black drum fish (*P. cromis*) are marked with black circles.
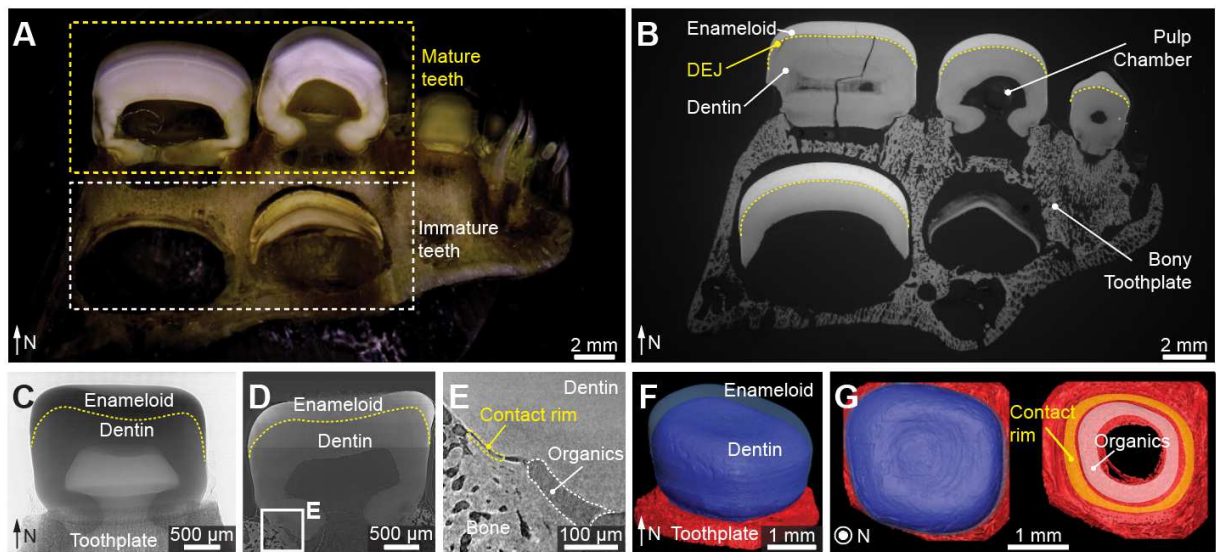
Figure 2 (full width)

Fig. 2. Macroscale structure of black drum fish teeth. (A) Optical microscopy image of a horizontally-cut and polished cross-section of an UPJ, showing the two layers of teeth, outer (exposed) mature teeth and inner (embedded) immature teeth. **(B)** Scanning electron micrograph (SEM) of an UPJ cross-section in backscatter mode, highlighting the two-layered structure in each tooth, higher mineralized enameloid (outer brighter) and less mineralized dentin (inner darker) intersected by the dentin-enameloid junction (DEJ) interface. **(C-E)** Synchrotron-based X-ray micro-tomography (μCT) results of a mature tooth, including **(C)** the projection image and **(D)** a reconstruction slice, respectively, where **(E)** magnifies the contact rim (yellow dashed region) and fibrous organics (white dashed area) between dentin and bone. **(F,G)** 3D reconstruction based on the μCT results, including **(F)** enameloid set in transparent mode, and **(G)** top-views of the tooth showing the "molar" tooth surface and the limited contact rim (yellow) and regions of organics (white) between tooth and bone.
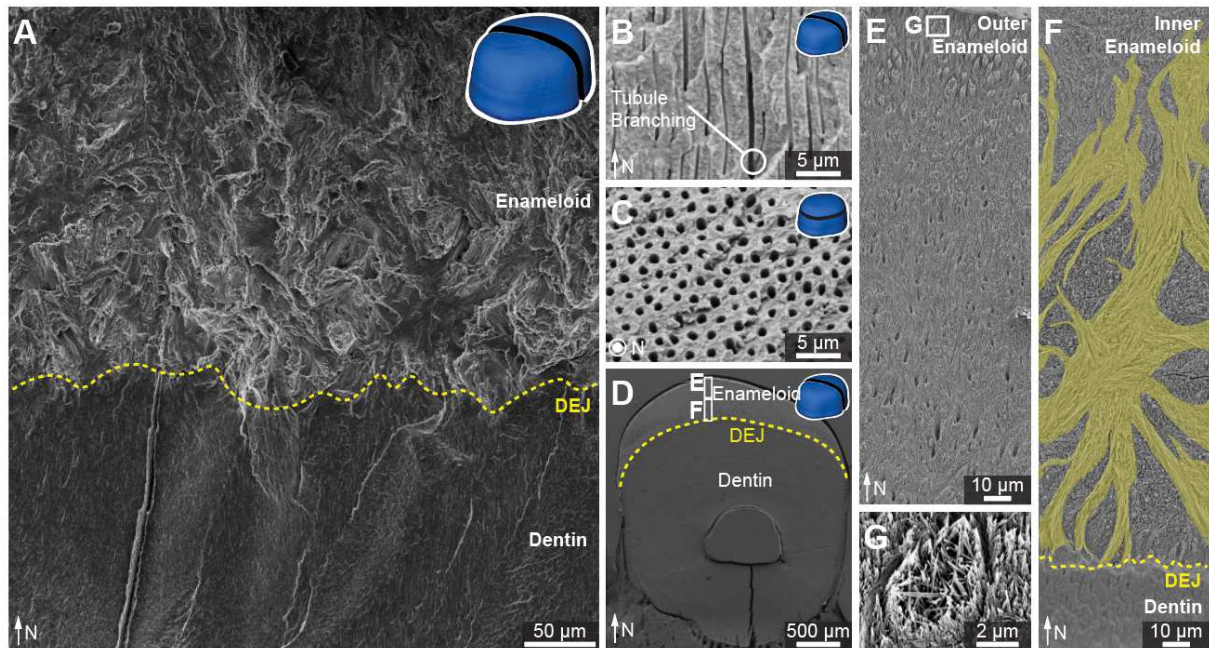
Figure 3 (full width)

Fig. 3. Microstructure of black drum fish teeth. (A) The Fracture surface of a mature tooth, revealing different microstructures in the enameloid and dentin. (B,C) Fracture surfaces of the dentin layer along the (B) vertical and (C) horizontal directions, respectively. (D) SEM image of a polished and etched mature tooth sample along the vertical cross-section. (E,F) High-magnification SEM images of the slightly etched tooth enameloid, revealing the microstructures of the (E) outer and (F) inner enameloid region, respectively. The yellow-shaded region in (F) highlights the twisted morphology of enameloid rods. (G) High-resolution SEM image near the tooth's surface, showing the needle-like crystallites in enameloid rods.
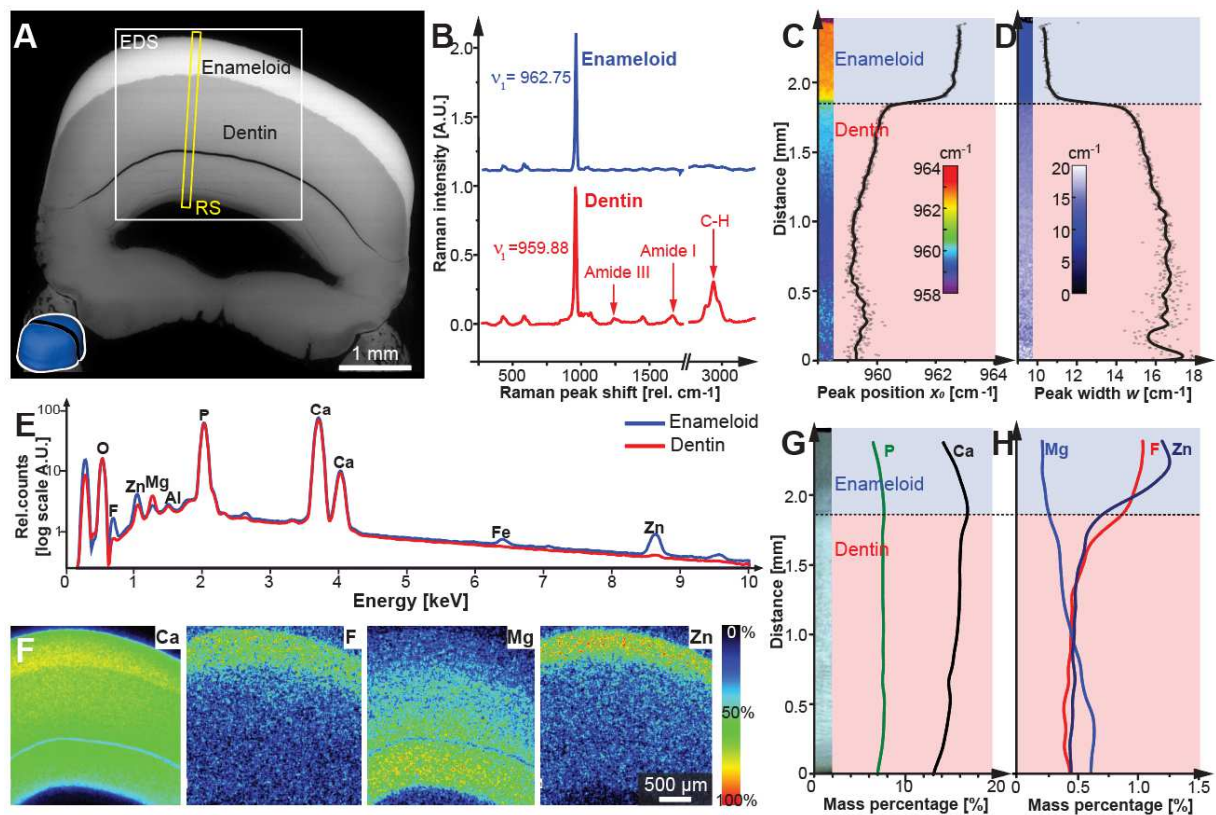
Figure 4 (full width)

Fig. 4. Chemical composition and Raman spectroscopy of the black drum fish teeth. **(A)** SEM image of a polished mature tooth, where the yellow and white boxes indicate the regions for Raman spectroscopy (RS) and Energy-dispersive X-ray spectroscopy (EDS) measurements, respectively. Note that a crack was formed due to the vacuum environment during the SEM/EDS measurement, which was not present during the initial RS measurement. **(B)** Average Raman spectra of enameloid (blue) and dentin (red). The most prominent peaks are marked, and the positions of phosphate v_1 peak are annotated. **(C,D)** Raman spectra results regarding **(C)** peak position and **(D)** full width at half maximum (FWHM) of the phosphate v_1 peak *vs*. position along the scanned column. **(E)** Average EDS spectra of enameloid (blue) and dentin (red). **(F)** EDS map of the representative elements (F, Ca, Mg, and Zn) on the scanned area. **(G,H)** Mass percentage of **(G)** major elements (Ca and P) and **(H)** trace elements (Mg, Zn, and F) in the mature tooth based on EDS measurements.
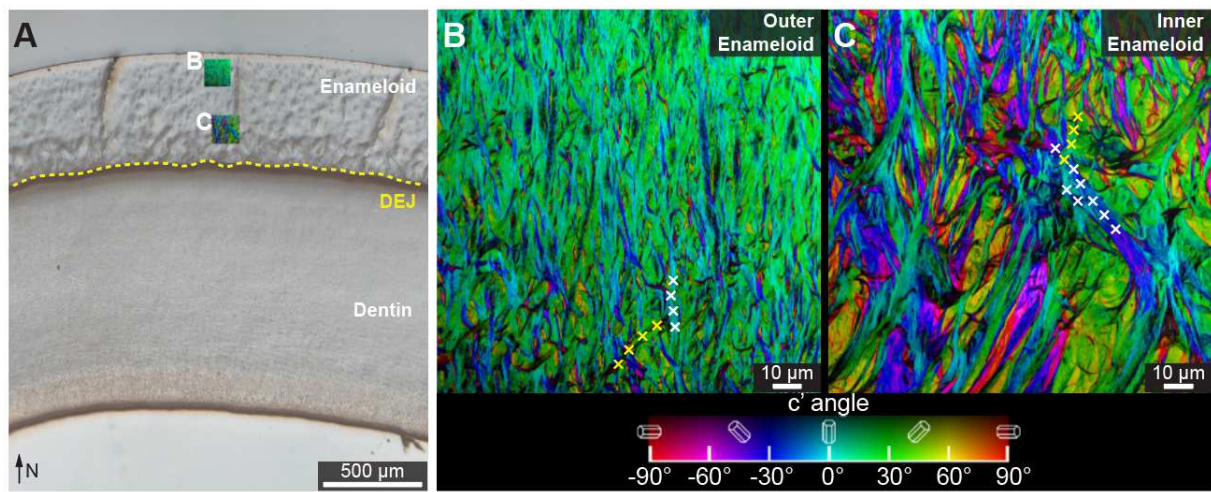
Figure 5 (full width)

Fig. 5. Polarization-dependent imaging contrast (PIC) maps on the outer and inner enameloid regions of the black drum fish teeth. (A) Visible light micrograph of embedded and polished black drum tooth, where the PIC maps were acquired on the two square regions (*ca.* 130 μm × 130 μm) of outer and inner enameloid, respectively. **(B,C)** PIC maps showing the different hydroxyapatite/fluorapatite (HA/FA) crystal sizes and orientations in **(B)** outer enameloid and **(C)** inner enameloid, respectively. The crystal orientations are color-coded as shown in the schematic apatite prisms, where the crystal *c*-axes are seen in projection perpendicular to the X-ray beam. The white and yellow crosses mark representative interwoven rods in the enameloid.
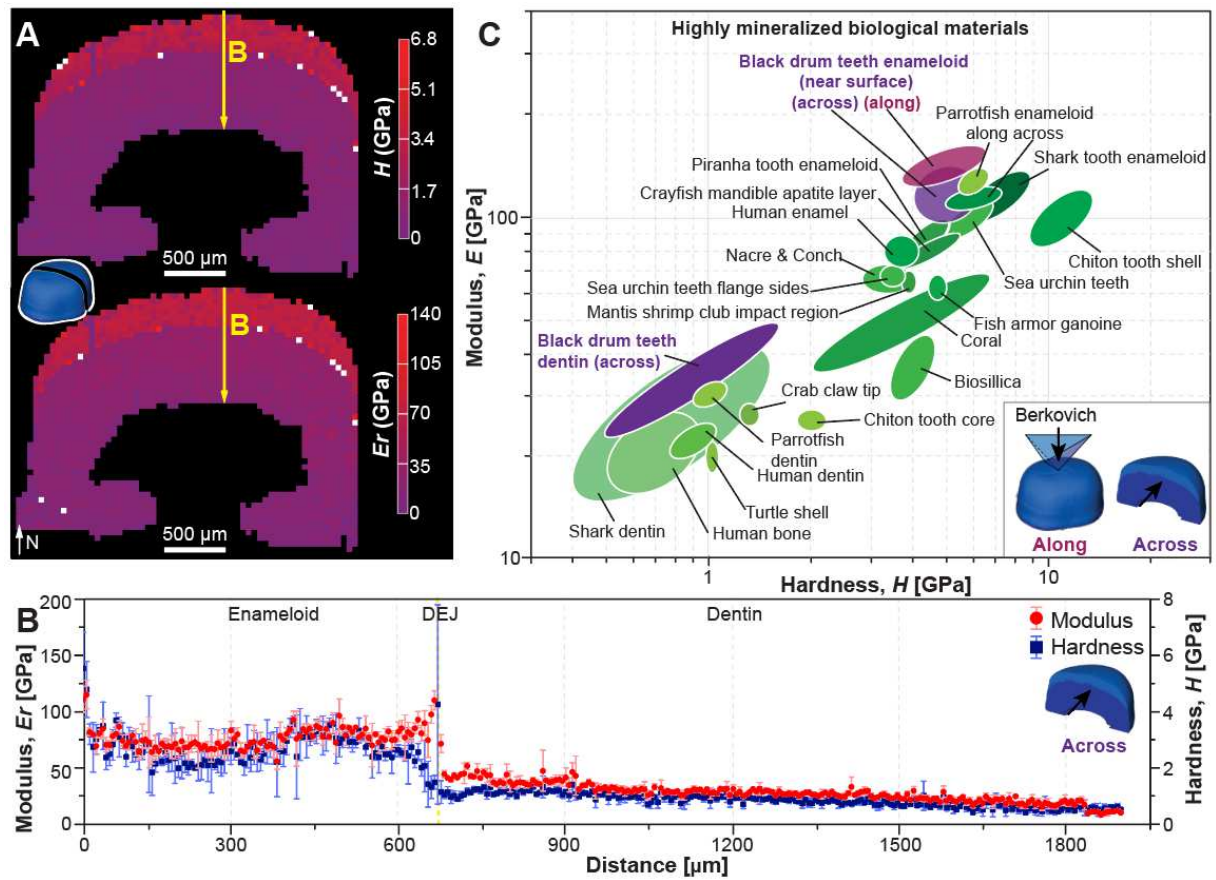
Figure 6 (full width)

Fig. 6. Nanoindentation properties of the black drum fish teeth. (**A**) Nanoindentation mapping results (hardness *H*, and reduced modulus E_r) on the vertical cross-section of a mature teeth (across the biting direction). (**B**) Fine line-mapping nanoindentation along the tooth thickness (yellow arrow in (**A**)), showing the local variation of the indentation properties. (**C**) Ashby plot of modulus *E* vs. hardness *H*, including the properties of the black drum fish tooth enameloid and dentin measured along and across the biting direction (see illustration at the bottom right corner). The Ashby plot in (**C**) was adapted from Refs. [36] and [52].
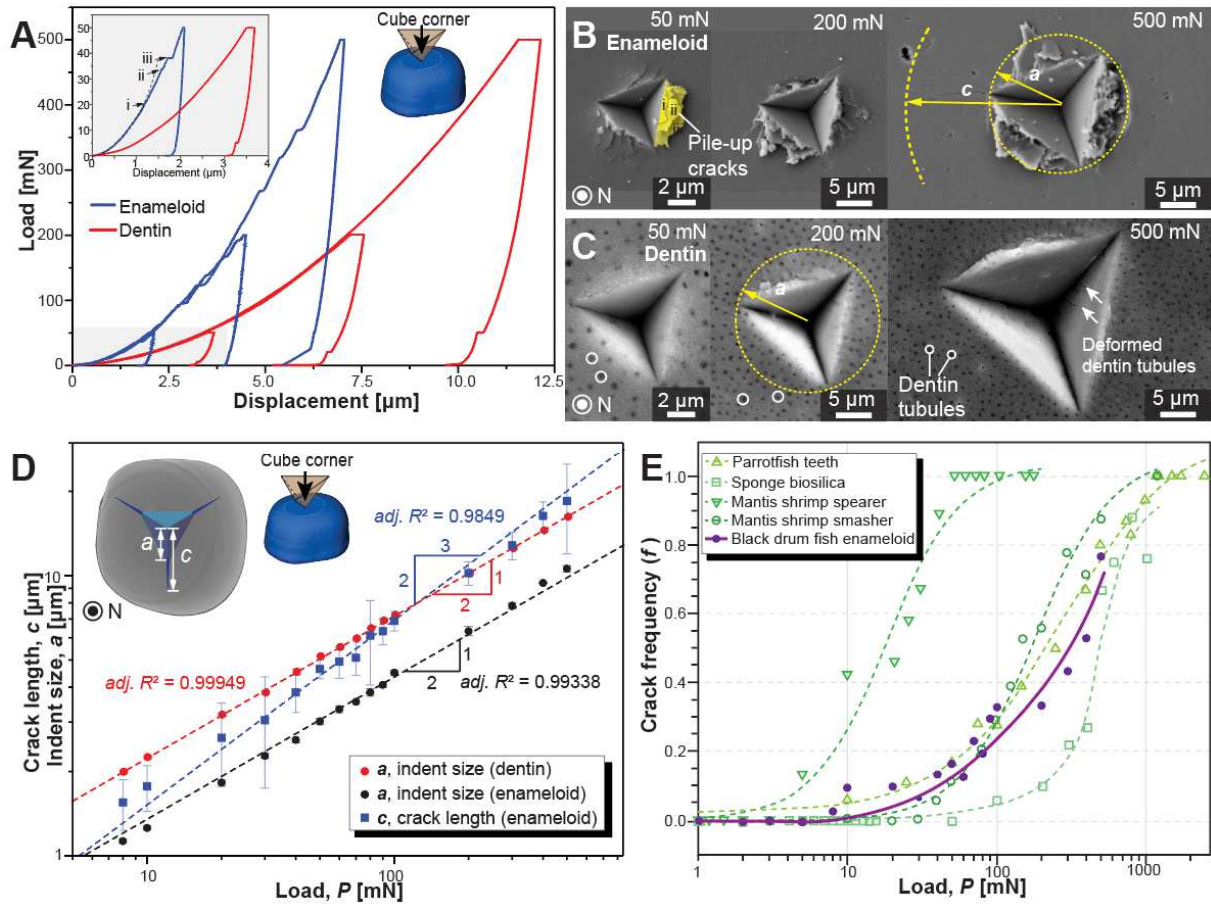
Figure 7 (full width)

Fig. 7. Nanoindentation fracture of the black drum fish's tooth enameloid and dentin. (A) Representative curves of cube-corner nanoindentations on the enameloid and dentin at maximum loads of 50 mN, 200 mN, and 500 mN. The inset on the top left magnifies the 50 mN curves to illustrate the three pop-in events during the indentation on polished enameloid. (B,C) Post-indent SEM images of (C) the enameloid and (C) dentin corresponding to the curves in (A), respectively. The three pile-up cracks of the 50 mN indent on enameloid correspond to the three pop-in events in the inset of (A). (D) Correlative fittings of indentation load (cube-corner tip) P on the crack length c and indent size a. (E) Cracking efficiency in the black drum fish's tooth enameloid in comparison to other biomineralized composites, including the parrotfish teeth [36], mantis shrimp spearers and smashers [63], and sponge biosilica [56].
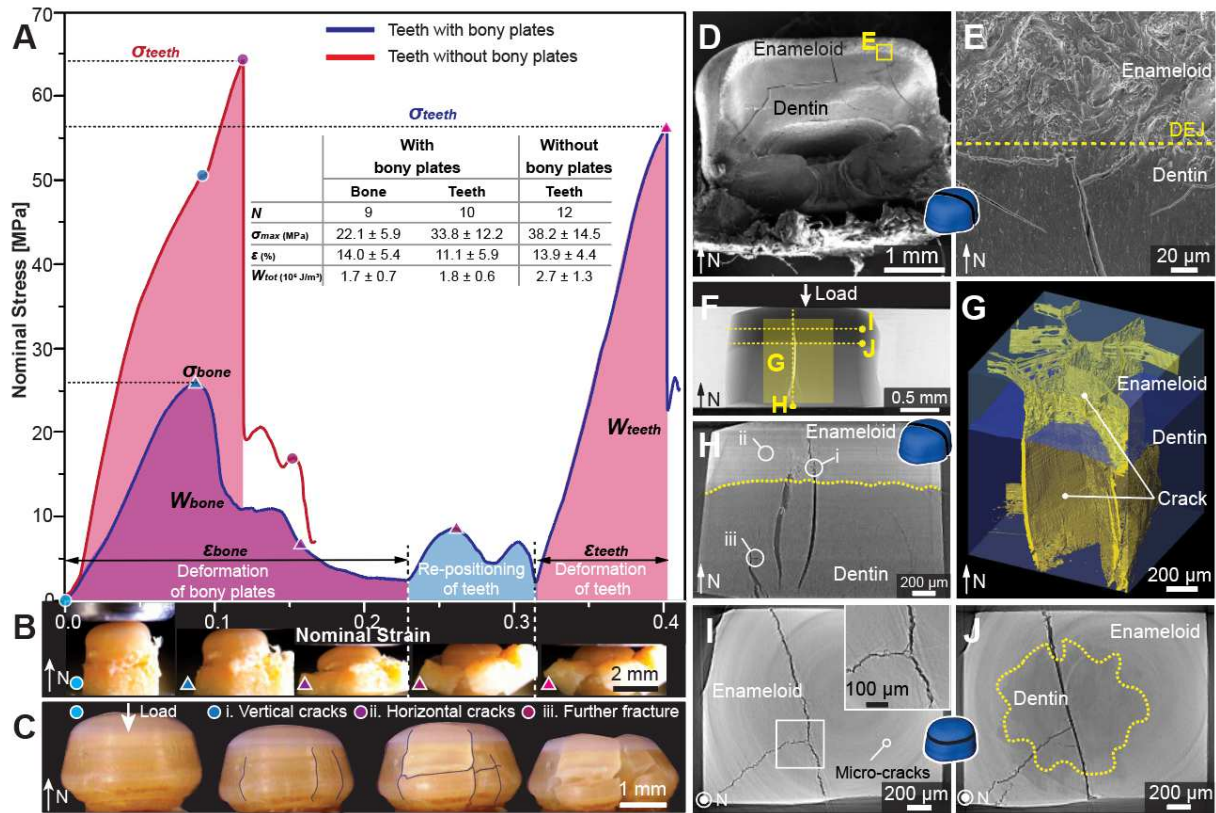
29

Figure 8 (full width)

Fig. 8. Mechanical performance of individual tooth of black drum fish teeth. (A) Representative nominal stress-strain curves of mature teeth (with and without bony foundation) under compression, where the teeth samples were considered as irregular-shaped pillars with uniform cross-section. (B,C) Representative deformation steps of the mature tooth (B) with and (C) without bony toothplate, indicated by triangles and circles on the stress-strain curves, respectively. The cracks on the tooth surface in the non-bone sample are highlighted with solid lines. (D) SEM image of a fractured tooth (with toothplate) after compression failure. (E) High magnification SEM image of the fractured surface near the DEJ boundary. (F) A representative projection of the tooth sample during *in-situ* compression tests. (G) 3D reconstruction of the selected volume (shaded in yellow in (F)), where the enameloid and dentin layer is shown in transparent mode to reveal the 3D crack. (H) Selected vertical reconstruction slice across the cracking regions, where the circled regions indicate (i) decussation of the inner enameloid, (ii) micro-cracks impeded when approaching the inner enameloid, and (iii) crack deflection in inner dentin. (I,J) Selected transverse reconstruction slices at the heights of (I) the middle enameloid and (J) DEJ, where the inset in (I) highlights the crack intersections.
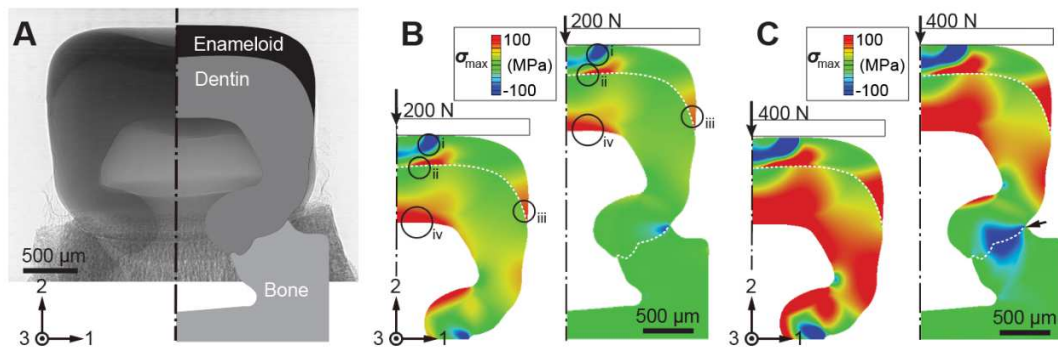
Figure 9 (full width)

Fig. 9. Finite Element (FE) simulations on the overall performance of black drum fish teeth. (A) 2D FE model simplified from the projection image of a mature tooth, where the interfaces of DEJ and dentin-bone are considered as perfect bonding. **(B,C)** FE results comparing the distribution of the maximum principal stress (σ_{max}) on the tooth with and without bony foundation under compressive loading of **(B)** 200 N, and **(C)** 400 N, where the direction 1,2,3 represent the radial, vertical, and circumferential directions, respectively. The arrow in **(C)** highlights the failure initiation near the dentin-bone surface.